

# Learning classical density functionals for ionic fluids

Anna T. Bui<sup>1</sup> and Stephen J. Cox<sup>2,\*</sup>

<sup>1</sup>Yusuf Hamied Department of Chemistry, University of Cambridge,  
Lensfield Road, Cambridge, CB2 1EW, United Kingdom

<sup>2</sup>Department of Chemistry, Durham University, South Road, Durham, DH1 3LE, United Kingdom  
(Dated: October 4, 2024)

Accurate and efficient theoretical techniques for describing ionic fluids are highly desirable for many applications across the physical, biological and materials sciences. With a rigorous statistical mechanical foundation, classical density functional theory (cDFT) is an appealing approach, but the competition between strong Coulombic interactions and steric repulsion limits the accuracy of current approximate functionals. Here, we extend a recently presented machine learning (ML) approach [Sammüller *et al.*, Proc. Natl. Acad. Sci. USA, **120**, e2312484120 (2023)] designed for systems with short-ranged interactions to ionic fluids. By adopting ideas from local molecular field theory, the framework we present amounts to using neural networks to learn the local relationship between the one-body direct correlation functions and inhomogeneous density profiles for a “mimic” short-ranged system, with effects of long-ranged interactions accounted for in a mean-field, yet well-controlled, manner. By comparing to results from molecular simulations, we show that our approach accurately describes the structure and thermodynamics of the prototypical model for electrolyte solutions and ionic liquids: the restricted primitive model. The framework we present acts as an important step toward extending ML approaches for cDFT to systems with accurate interatomic potentials.

The behavior of ionic fluids underlies a vast array of physical and biological phenomena as well as technological applications, ranging from electrolyte solutions controlling protein folding [1] to room-temperature ionic liquids in energy storage devices [2]. A fundamental topic that continues to attract enormous interest both experimentally [3–7] and theoretically [8–13] is the structure and thermodynamics of ions near charged interfaces, in particular, how the nature of both the electrolyte and solid surface impacts the properties of the electric double layer (EDL). Poisson–Boltzmann (PB) theory and its linearized Debye–Hückel form provide the basis for much of our understanding of ionic fluids. Their neglect of correlations arising from nonelectrostatic interactions, however, restricts their validity to fluids of low ionic strength.

Classical density functional theory (cDFT) [14–17] provides a natural framework for including correlations omitted by PB theory, and has proven to be a powerful approach to describe equilibrium structure and thermodynamics of fluids in general. While in principle an exact theory, historically, cDFT relies on making approximations for the excess intrinsic free energy functional  $\mathcal{F}_{\text{intr}}^{(\text{ex})}[\{\rho_\nu\}]$ , where  $\rho_\nu$  denotes the one-body density of species  $\nu$ . For hard sphere fluids, functionals based on Rosenfeld’s fundamental measure theory (FMT) [18–21] have proven highly successful. For simple liquids with square-well, Yukawa, or Lennard–Jones interaction potentials, hard sphere mixtures act as suitable reference systems, with effects of attractive interactions described reasonably well in a mean-field fashion [22–24]. In contrast, existing functionals for ionic fluids are far less accurate, failing to adequately capture the interplay between Coulombic and steric interactions [25–28]. In this Letter, we present a strategy that utilizes machine learning (ML) to construct accurate free energy functionals for ionic fluids.

The rapid advance of modern ML approaches means there has been much recent interest in “learning” representations of the exact  $\mathcal{F}_{\text{intr}}^{(\text{ex})}[\{\rho_\nu\}]$  [29–35]. Here we build on the method proposed by Sammüller *et al.* [36], in which the one-body direct correlation functions,

$$c_\nu^{(1)}(\mathbf{r}; [\{\rho_\nu\}]) = -\frac{\beta \delta \mathcal{F}_{\text{intr}}^{(\text{ex})}[\{\rho_\nu\}]}{\delta \rho_\nu(\mathbf{r})}, \quad (1)$$

are learned by generating inhomogeneous density profiles in the presence of various external- and chemical potentials by grand canonical (GC) simulations. This approach to cDFT, dubbed “neural functional theory,” has been shown to outperform FMT-based approaches for both hard sphere fluids and Lennard–Jones liquids in terms of both accuracy and speed [36, 37].

Two key features underpin the success of the neural functional approach: (i) the feasibility of GC simulations to produce inhomogeneous density profiles of sufficient quality to form a reliable training set; and (ii) short-ranged (SR) correlations such that the functional relationship between  $c_\nu^{(1)}$  and  $\{\rho_\nu\}$  is local. Ionic fluids pose challenges on both fronts. First, GC simulations for ionic systems raise delicate questions concerning electroneutrality, with various schemes proposed that either insert individual ions or neutral pairs [38–42]. Even then, simulations corresponding exactly to the GC ensemble where the number of each species can fluctuate are impractical, owing to poor acceptance rates of trial insertion and deletion moves. Second, the long-ranged (LR) nature of the Coulomb potential leads to a nonlocal relationship between  $c_\nu^{(1)}$  and  $\{\rho_\nu\}$ . We circumvent both of these issues by adopting concepts from local molecular field theory (LMFT) [43–47], which has been shown to have close links to cDFT [48].

We focus our efforts on the prototypical model of an ionic

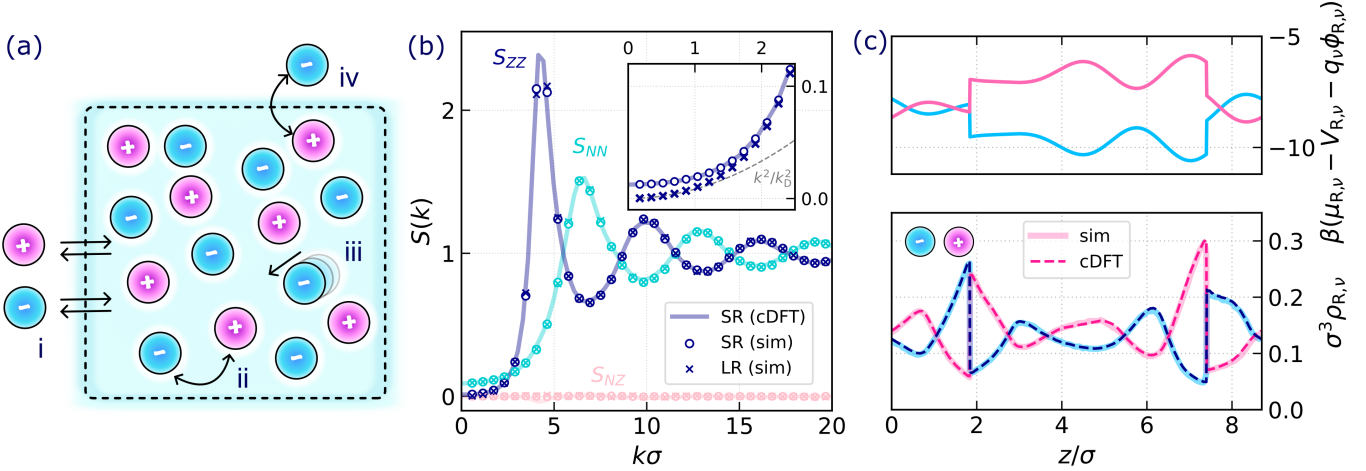


**Figure 1: Structure of the SR mimic RPM.** (a) Training data for the neural functional are obtained from GCMC simulations with (i) insertion/deletion, (ii) position swapping, (iii) displacement and (iv) mutation (identity exchange) moves. (b) The static structure factors from cDFT agree well with results from molecular simulation across the whole range of  $k$  for the SR system, shown for a bulk system with  $\sigma^3 \rho_{R,\pm} = 0.315$ . Inset: At low  $k$ , the SR system violates the perfect screening condition, whereas the LR system obeys the Stillinger-Lovett sum rule (see Eq. 5). (c) For the applied external potentials (top), predictions of the ion density profiles (bottom) are in excellent agreement with the simulation data.

fluid: the restricted primitive model (RPM) comprising oppositely charged hard spheres of equal diameter  $\sigma$ , embedded in a uniform dielectric continuum. The scheme we propose can be briefly summarized. First, by employing neural networks, we find the one-body direct correlation functions for a suitably chosen “mimic system” whose electrostatic interactions are entirely short-ranged. Then, by leveraging LMFT and its relation to cDFT, we account for the net averaged effects of LR electrostatic interactions in a well-controlled fashion. When compared to molecular simulations, the framework we outline describes inhomogeneous density profiles, the equation of state, and the properties of the electric double layer in the presence of electric fields with very high accuracy.

**cDFT of a short-ranged “mimic” ionic fluid.** Our overall strategy follows that of LMFT, in which we consider a suitably chosen mimic system whose interatomic interactions are entirely short-ranged, and, when subject to a suitably chosen one-body potential  $\phi_R$ , has the same one-body densities as the system of interest with LR interactions (the “full” system). For systems such as the RPM, where LR interactions arise from the Coulomb potential, one adopts the exact splitting

$$1/r = v_0(r) + v_1(r), \quad (2)$$

with  $v_0(r) = \text{erfc}(\kappa r)/r$  and  $v_1(r) = \text{erf}(\kappa r)/r$ . The interatomic potential of the mimic system is then  $v_0$ , and the length scale  $\kappa^{-1}$  is chosen such that the mimic system accurately describes the SR correlations of the full system. In the following, we will work with  $\kappa^{-1} = 1.8\sigma$  (see the SM [49]). We will also indicate quantities pertaining to the mimic system with a subscript “R” and focus on behaviors at a reduced temperature  $T^* = 0.066$ , corresponding to su-

percritical conditions [50]. The one-body direct correlation functions of the mimic system can be exactly written as

$$c_{R,\nu}^{(1)}(\mathbf{r}) = \ln \Lambda_\nu^3 \rho_{R,\nu}(\mathbf{r}) + \beta V_{R,\nu}(\mathbf{r}) + \beta q_\nu \phi_R(\mathbf{r}) - \beta \mu_{R,\nu}, \quad (3)$$

where  $\Lambda_\nu$ ,  $\mu_{R,\nu}$  and  $q_\nu$  indicate the thermal de Broglie wavelength, chemical potential and point charge of species  $\nu$ , respectively,  $V_{R,\nu}$  encompasses any non-electrostatic contributions to the external potential for species  $\nu$  and, for now,  $\phi_R$  is a general external electrostatic potential; we will later discuss how  $\phi_R$  can be chosen such that  $\rho_{R,\nu}(\mathbf{r}) = \rho_\nu(\mathbf{r})$ .

To learn the functional relationship for  $c_{R,\nu}^{(1)}(\mathbf{r}; \{\rho_{R,\nu}\})$ , we obtain data for the right hand side of Eq. 3 by measuring  $\rho_{R,\nu}$  from simulations with known  $\beta V_{R,\nu}$ ,  $\beta \phi_R$  and  $\beta \mu_{R,\nu}$ . To this end, in line with Ref. 36, we perform simulations in a planar geometry at different combinations of  $\{\beta V_{R,\nu}\}$ ,  $\beta \phi_R$  and  $\{\beta \mu_{R,\nu}\}$ . The form of  $v_0$  means that each particle of the mimic system can be considered electroneutral, comprising both a point charge and a compensating Gaussian charge distribution [51]. As such, in addition to translational moves, we can readily perform GC particle insertions/deletions, along with semi-GC swapping of “anions” and “cations” without needing to worry about issues of electroneutrality (see Fig. 1(a)). We have found this highly beneficial to converging our simulations, full details of which are provided in the SM [49].

For each species,  $\nu = +$  or  $-$ , the neural network used to represent the relationship  $\{\rho_{R,\nu}(z)\} \rightarrow c_{R,\nu}^{(1)}(z)$  is structured as follows. The input layer has two channels which are supplied with the discretized values of the cation and anion density profiles in a window  $\Delta z = 3.6\sigma$  around the particular value of  $z$ . Following a fully-connected multi-layer perceptron of three layers, the output layer consists of a single node, which yields the predicted value of  $c_{R,\nu}^{(1)}$  at

position  $z$ . For the SR mimic RPM, we train two independent networks, one for the cation and one for the anion. To reduce noise in the bulk structure predictions, we also obtained models regularized with bulk two-body direct correlation functions as proposed in Ref. 52. Details of our training procedure are provided in the SM [49], and all data are openly available.

We first assess the bulk structure predicted by the functional. On the basis of the neural network, we make use of automatic differentiation and radial projection to obtain the partial two-body direct correlation functions  $c_{\nu\lambda}^{(2)}(r)$  (see Ref. [36] and the SM [49]). By solving the general Ornstein-Zernike equation for mixtures [53, 54], we then obtain the total correlation functions  $h_{\nu\lambda}^{(2)}(r)$  and the corresponding structure factors  $S_{\nu\lambda}(k)$ . We further quantify the degree of coupling between number-number ( $S_{NN}$ ), number-charge ( $S_{NZ}$ ) and charge-charge ( $S_{ZZ}$ ) densities by appropriate weighted summations

$$\begin{aligned} S_{NN}(k) &= S_{++}(k) + 2S_{+-}(k) + S_{--}(k), \\ S_{NZ}(k) &= S_{++}(k) - S_{--}(k), \\ S_{ZZ}(k) &= S_{++}(k) - 2S_{+-}(k) + S_{--}(k). \end{aligned} \quad (4)$$

Fig. 1(b) shows that the static structure factors obtained from the functional are in excellent agreement with results from a molecular dynamics (MD) simulation of the mimic system at the same bulk densities. The symmetry of the RPM is well-captured, reflected in  $S_{NZ}(k) = 0$ . Moreover, by comparing to results from a MD simulation of the full system, we see that  $S_{NN}(k)$  and  $S_{ZZ}(k)$  for the full and mimic systems agree very well at sufficiently large  $k$ , confirming that our choice of  $\kappa^{-1} = 1.8\sigma$  is sufficient for the mimic system to capture the SR correlations of the full system. Deviations of the SR system from the LR system only manifest significantly in  $S_{ZZ}(k)$  at small  $k$ , in agreement with previous works on the subject [46, 55]. In particular, as shown in the inset, we see that  $S_{ZZ}(k)$  for the LR system strictly obeys the Stillinger-Lovett sum rule [56, 57]

$$\lim_{k \rightarrow 0} \frac{k_D^2}{k^2} S_{ZZ}(k) = 1, \quad (5)$$

where  $k_D^{-1}$  is the Debye screening length. In contrast, for the mimic system we observe  $S_{ZZ}(k) > k^2/k_D^2$  as  $k \rightarrow 0$ , indicative of a lack of screening. Consistent with the dielectric response of a short-ranged water model [55], these deviations appear at length scales far larger than the range separation prescribed by  $2\pi\kappa = 3.5\sigma^{-1}$ .

Turning to the ability of cDFT to predict inhomogeneous structure, the equilibrium density profiles of the mimic system can be obtained by self-consistently solving the Euler-Lagrange equation

$$\begin{aligned} \Lambda_{\nu}^3 \rho_{R,\nu}(\mathbf{r}) &= \exp \left( -\beta V_{R,\nu}(\mathbf{r}) - \beta q_{\nu} \phi_R(\mathbf{r}) \right. \\ &\quad \left. + \beta \mu_{R,\nu} + c_{R,\nu}^{(1)}(\mathbf{r}; \{\rho_{\nu}\}) \right), \end{aligned} \quad (6)$$

where  $c_{R,\nu}^{(1)}$  is evaluated by the corresponding neural network. As shown in Fig. 1(c) for a representative set of external potentials, the resulting  $\{\rho_{R,\nu}(z)\}$  from cDFT are in excellent agreement with reference simulation data of the mimic system.

**Accounting for long-ranged electrostatics with LMFT.** Having established that the cDFT obtained from the ML procedure is accurate for a SR variant of the RPM, we turn our attention to incorporating the effects of LR electrostatic interactions. To do so, we will use concepts from LMFT. The premise of LMFT is that there exists a potential  $\phi_R$  such that

$$\rho_{\nu}(\mathbf{r}; [\phi], \{\mu_{\nu}\}) = \rho_{R,\nu}(\mathbf{r}; [\phi_R], \{\mu_{R,\nu}\}). \quad (7)$$

In Eq. 7, we have explicitly indicated the functional dependence of the densities on the external electrostatic potential [58]. As shown in Ref. 48, when recast in a cDFT framework, LMFT relates the one-body direct correlation functions of the full and mimic systems through

$$c_{\nu}^{(1)}(\mathbf{r}; \{\rho_{\nu}\}) = c_{R,\nu}^{(1)}(\mathbf{r}; \{\rho_{\nu}\}) - \beta \Delta \mu_{\nu} - \beta q_{\nu} \Delta \phi(\mathbf{r}), \quad (8)$$

which is an exact result. A key insight from LMFT [43, 44] is that for an appropriate splitting of the potential (see Eq. 2),  $\Delta \phi$  is well-approximated by a mean field form

$$\Delta \phi(\mathbf{r}) \equiv \phi(\mathbf{r}) - \phi_R(\mathbf{r}) = -\frac{1}{\epsilon} \int d\mathbf{r} n(\mathbf{r}) v_1(|\mathbf{r} - \mathbf{r}'|), \quad (9)$$

where  $\epsilon$  is the dielectric constant of the continuum and  $n = n_R = \sum_{\nu} q_{\nu} \rho_{\nu}$  is the charge density. For homogeneous systems, Rodgers and Weeks have also derived a thermodynamic correction for the total energy, from which a correction for the pressure follows [59],

$$\Delta P \equiv P - P_R = -\frac{k_B T}{2\pi^{3/2} \kappa^{-3}}. \quad (10)$$

Based on Ref. 59, we have further derived a correction for the chemical potential (see the SM [49]),

$$\Delta \mu_{\nu} \equiv \mu_{\nu} - \mu_{R,\nu} = -\frac{q_{\nu}^2}{\kappa^{-1} \sqrt{\pi}}. \quad (11)$$

We first consider the bulk thermodynamics of the RPM. The equation of state for the LR system is obtained with

$$P(\{\rho_{\nu}\}) = \sum_{\nu} k_B T \rho_{\nu} \left( 1 - c_{R,\nu}^{(1)}[\rho_{\nu}] \right) - \frac{\mathcal{F}_{\text{intr},R}^{(\text{ex})}[\{\rho_{\nu}\}]}{V} + \Delta P, \quad (12)$$

where the sum of the first two terms is the negative of the grand potential density of the mimic system. The excess free energy  $\mathcal{F}_{\text{intr},R}^{(\text{ex})}$  is accessible by functional line integration. The result of this procedure, shown in Fig. 2(a), agrees very well with reference simulation data. We also see that, particularly at higher densities, Eq. 12 performs significantly better than the analytical approximation that

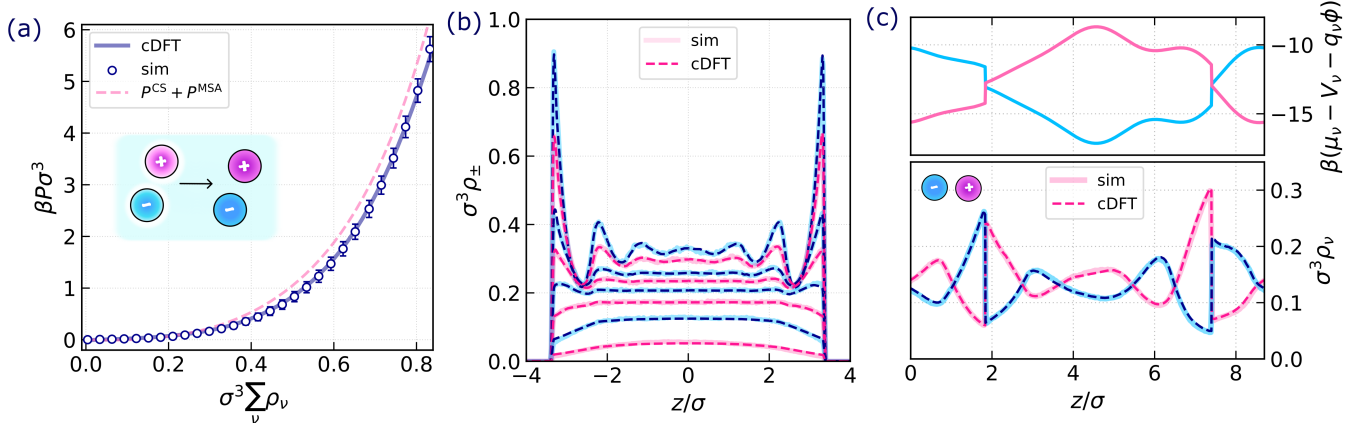


**Figure 2: Structure and thermodynamics of the LR full system.** cDFT for the RPM at  $T^* = 0.066$  with effects of LR electrostatic interactions accounted by LMFT shows excellent agreement with reference molecular simulation data for (a) the equation of state, (b) ion density profiles confined in a slit and (c) with an applied external potential. In (a), we see that our cDFT approach outperforms the prediction obtained by combining the Carnahan–Starling equation of state for hard-sphere fluids ( $P^{\text{CS}}$ ) and the mean spherical approximation ( $P^{\text{MSA}}$ ). For the LR system in (c), the applied external potential acts over a much longer range and the chemical potentials are shifted lower compared to the SR mimic system in Fig. 1(c) to yield  $\rho_{\nu}(z) = \rho_{R,\nu}(z)$ .

results from adding the Carnahan–Starling equation of state ( $P^{\text{CS}}$ ) [60] and the mean spherical approximation ( $P^{\text{MSA}}$ ) [61, 62], despite the fact that  $P^{\text{CS}} + P^{\text{MSA}}$  forms the basis for the vast majority of current state-of-the-art functionals for ionic fluids [27, 28].

The advantages of cDFT combined with LMFT become even clearer when inhomogeneous systems are considered. The equilibrium densities of the full system are given by

$$\Lambda_{\nu}^3 \rho_{\nu}(\mathbf{r}) = \exp \left( -\beta V_{\nu}(\mathbf{r}) - \beta q_{\nu} \phi(\mathbf{r}) + \beta \mu_{\nu} + c_{\nu}^{(1)}(\mathbf{r}; \{\rho_{\nu}\}) \right), \quad (13)$$

where the non-local functional  $c_{\nu}^{(1)}$  is now given by Eq. 8, together with Eq. 9 and Eq. 11. From a cDFT perspective, we have captured all strong rapidly-varying short-ranged correlations with the neural networks for  $c_{R,\nu}^{(1)}$ , while the effects of LR electrostatic interactions are incorporated in a mean-field, yet well-controlled fashion.

In practical terms, for a planar geometry, Eq. 9 can be recast as

$$\Delta \phi(z) = -\frac{1}{\epsilon L} \sum_{k \neq 0} \frac{4\pi}{k^2} \tilde{n}(k) \exp(ikz) \exp \left( -\frac{k^2}{4\kappa^2} \right), \quad (14)$$

where  $\tilde{n}$  denotes a Fourier component of  $n$ , and  $L$  is the total length of the periodic cell. In Fig. 2(b), we show the results from our cDFT approach for the RPM confined between two repulsive walls for various values of  $\mu_+ = \mu_-$ . The density profiles are in very good agreement with reference canonical MD simulation data in which the number of particles matches that obtained by integrating the density profiles from cDFT. Our cDFT approach also works very well in cases where the external potential contains an electrostatic component, as illustrated in Fig. 2(c). Here, the

full system is the LR counterpart of the mimic system shown in Fig. 1(c), emphasizing the premise of LMFT (see Eq. 7).

**The electric double layer.** The results presented so far demonstrate that our cDFT approach provides an efficient and accurate route to the structure and thermodynamics of bulk and inhomogenous ionic fluids. As an application, we turn our attention to the fundamental topic of ongoing scientific interest: the electric double layer.

As a simple model of an EDL-forming system, we consider the RPM confined between two repulsive walls, and in the presence of an electric field  $E_z$  along the  $z$  direction. The electrostatic potential that the LR system feels is  $\phi(z) = -E_z z$ , as depicted in Fig. 3(a). As pointed out in previous applications of LMFT [63], the SR mimic system in this case feels the electrostatic potential  $\phi_R$  due to smooth planar Gaussian charge distributions at the walls, as depicted in Fig. 3(b). For the reference simulation data, the LR system was simulated at constant  $E_z$  using the finite-field approach [64–70]. As shown in Fig. 3(c), the ion distributions from our cDFT approach are in excellent agreement with the results from simulation. As a significant advancement in theoretical descriptions of the EDL, our cDFT approach can accurately describe the strong oscillations in the density profiles of co- and counter-ions. Moreover, as we detail in the SM [49], our functional is thermodynamically consistent, satisfying the contact density theorem [71–73]

$$P = - \sum_{\nu} \int dz \rho_{\nu}(z) \frac{dV_{\nu}(z)}{dz} - \frac{2\pi\sigma_s^2}{\epsilon}, \quad (15)$$

which relates the bulk pressure to the surface charge density  $\sigma_s = \int_{-L}^0 dz n(z)$  [74] and ion densities at contact with the walls. Obeying this contact theorem has proven a challenge for most state-of-the-art cDFT functionals for ionic fluids [75, 76].

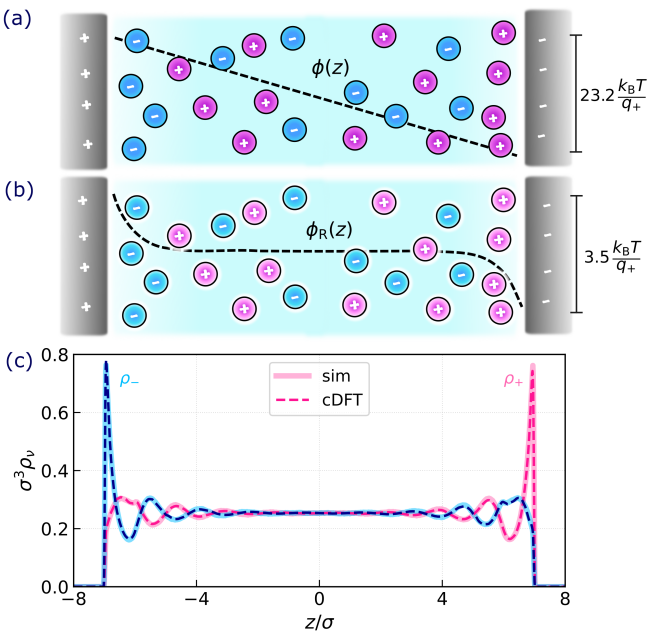


**Figure 3: Accurately describing the EDL with cDFT.** For the RPM confined between two repulsive walls and in the presence of an electric field, the potentials experienced by the full and mimic systems are shown in (a) and (b), respectively. The resulting ion density profiles from cDFT are in excellent agreement with molecular simulations, and obey the contact theorem (Eq. 15).

The main advantage of the neural functional approach outlined in Ref. 36 is arguably that the local relationship between  $c_\nu^{(1)}$  and  $\{\rho_\nu\}$  permits application of the resulting functional to system sizes far beyond those encountered during training of the ML. By using the framework of LMFT and its relationship to cDFT, we have successfully extended the neural functional approach to a case where the relationship between  $c_\nu^{(1)}$  and  $\{\rho_\nu\}$  is nonlocal. Future work will pursue using neural functionals to understand EDL capacitance [77] and surface force balance measurements [13], and to augment other cDFT approaches to understand solvation [78]. The framework we have outlined should also find use in describing the dielectric response of polar fluids such as water [55, 79, 80].

**Data availability.** Training data and code supporting the findings of this study will be openly available [81, 82].

**Acknowledgements.** Via membership of the UK's HEC Materials Chemistry Consortium funded by EPSRC (EP/X035859), this work used the ARCHER2 UK National Supercomputing Service. A.T.B. acknowledges funding from the Oppenheimer Fund and Peterhouse College, University of Cambridge. S.J.C. is a Royal Society University Research Fellow (Grant No. URF\R1\211144) at Durham University.

\* [stephen.j.cox@durham.ac.uk](mailto:stephen.j.cox@durham.ac.uk)

- [1] W. Kunz, J. Henle, and B. W. Ninham, 'Zur Lehre von der Wirkung der Salze' (about the science of the effect of salts): Franz Hofmeister's historical papers, *Curr. Opin. Colloid Interface Sci* **9**, 19 (2004).
- [2] S. Kondrat, G. Feng, F. Bresme, M. Urbakh, and A. A. Kornyshev, Theory and simulations of ionic liquids in nanoconfinement, *Chem. Rev* **123**, 6668 (2023).
- [3] R. M. Espinosa-Marzal, A. Arcifa, A. Rossi, and N. D. Spencer, Microslips to "avalanches" in confined, molecular layers of ionic liquids, *J. Phys. Chem. Lett* **5**, 179 (2014).
- [4] M. A. Gebbie, H. A. Dobbs, M. Valtiner, and J. N. Israelachvili, Long-range electrostatic screening in ionic liquids, *Proc. Natl. Acad. Sci. U.S.A* **112**, 7432 (2015).
- [5] A. M. Smith, A. A. Lee, and S. Perkin, The electrostatic screening length in concentrated electrolytes increases with concentration, *J. Phys. Chem. Lett* **7**, 2157 (2016).
- [6] A. A. Lee, C. S. Perez-Martinez, A. M. Smith, and S. Perkin, Underscreening in concentrated electrolytes, *Faraday Discuss* **199**, 239 (2017).
- [7] M. A. Gebbie, A. M. Smith, H. A. Dobbs, A. A. Lee, G. G. Warr, X. Banquy, M. Valtiner, M. W. Rutland, J. N. Israelachvili, S. Perkin, and R. Atkin, Long range electrostatic forces in ionic liquids, *Chem. Commun* **53**, 1214 (2017).
- [8] G. M. Torrie and J. P. Valleau, Electrical double layers. I. Monte Carlo study of a uniformly charged surface, *J. Chem. Phys* **73**, 5807 (1980).
- [9] C. Merlet, D. T. Limmer, M. Salanne, R. van Roij, P. A. Madden, D. Chandler, and B. Rotenberg, The electric double layer has a life of its own, *J. Phys. Chem. C* **118**, 18291 (2014).
- [10] M. Z. Bazant, B. D. Storey, and A. A. Kornyshev, Double layer in ionic liquids: Overscreening versus crowding, *Phys. Rev. Lett.* **106**, 046102 (2011).
- [11] F. Coupette, A. A. Lee, and A. Härtel, Screening lengths in ionic fluids, *Phys. Rev. Lett.* **121**, 075501 (2018).
- [12] J. P. de Souza, Z. A. H. Goodwin, M. McEldrew, A. A. Kornyshev, and M. Z. Bazant, Interfacial layering in the electric double layer of ionic liquids, *Phys. Rev. Lett.* **125**, 116001 (2020).
- [13] P. Cats, R. Evans, A. Härtel, and R. van Roij, Primitive model electrolytes in the near and far field: Decay lengths from DFT and simulations, *J. Chem. Phys* **154**, 124504 (2021).
- [14] R. Evans, The nature of the liquid-vapour interface and other topics in the statistical mechanics of non-uniform, classical fluids, *Adv. Phys* **28**, 143 (1979).
- [15] R. Evans, *Fundamentals of inhomogeneous fluids*, edited by D. Henderson (Dekker, New York, 1992).
- [16] J. F. Lutsko, *Recent Developments in Classical Density Functional Theory*, Adv. Chem. Phys. (John Wiley & Sons, 2010) pp. 1–92.
- [17] J. Hansen and I. McDonald, *Theory of Simple Liquids: with Applications to Soft Matter* (Elsevier Science, 2013).
- [18] Y. Rosenfeld, Free-energy model for the inhomogeneous hard-sphere fluid mixture and density-functional theory of freezing, *Phys. Rev. Lett.* **63**, 980 (1989).
- [19] R. Roth, R. Evans, A. Lang, and G. Kahl, Fundamental measure theory for hard-sphere mixtures revisited: the White Bear version, *J. Phys. Condens. Matter* **14**, 12063 (2002).
- [20] H. Hansen-Goos and R. Roth, Density functional theory for

hard-sphere mixtures: the White Bear version mark II, *J. Phys. Condens. Matter* **18**, 8413 (2006).

[21] R. Roth, Fundamental measure theory for hard-sphere mixtures: a review, *J. Phys. Condens. Matter* **22**, 063102 (2010).

[22] E. Kierlik and M. L. Rosinberg, Density-functional theory for inhomogeneous fluids: Adsorption of binary mixtures, *Phys. Rev. A* **44**, 5025 (1991).

[23] M. C. Stewart and R. Evans, Wetting and drying at a curved substrate: Long-ranged forces, *Phys. Rev. E* **71**, 011602 (2005).

[24] A. J. Archer, B. Chacko, and R. Evans, The standard mean-field treatment of inter-particle attraction in classical DFT is better than one might expect, *J. Chem. Phys* **147**, 034501 (2017).

[25] A. Härtel, M. Janssen, S. Samin, and R. v. Roij, Fundamental measure theory for the electric double layer: implications for blue-energy harvesting and water desalination, *J. Phys. Condens. Matter* **27**, 194129 (2015).

[26] A. Härtel, Structure of electric double layers in capacitive systems and to what extent (classical) density functional theory describes it, *J. Phys. Condens. Matter* **29**, 423002 (2017).

[27] R. Roth and D. Gillespie, Shells of charge: a density functional theory for charged hard spheres, *J. Phys. Condens. Matter* **28**, 244006 (2016).

[28] M. Bültmann and A. Härtel, The primitive model in classical density functional theory: beyond the standard mean-field approximation, *J. Phys. Condens. Matter* **34**, 235101 (2022).

[29] P. Cats, S. Kuipers, S. de Wind, R. van Damme, G. M. Coli, M. Dijkstra, and R. van Roij, Machine-learning free-energy functionals using density profiles from simulations, *APL Mater* **9**, 031109 (2021).

[30] J. Dijkman, M. Dijkstra, R. van Roij, M. Welling, J.-W. van de Meent, and B. Ensing, *Learning neural free-energy functionals with pair-correlation matching* (2024), arXiv:2403.15007 [cond-mat.soft].

[31] A. Simon and M. Oettel, *Machine learning approaches to classical density functional theory* (2024), arXiv:2406.07345 [cond-mat.stat-mech].

[32] S.-C. Lin, G. Martius, and M. Oettel, Analytical classical density functionals from an equation learning network, *J. Chem. Phys* **152**, 021102 (2020).

[33] L. Shang-Chun and M. Oettel, A classical density functional from machine learning and a convolutional neural network, *SciPost Phys.* **6**, 025 (2019).

[34] A. Malpica-Morales, P. Yatsyshin, M. A. Durán-Olivencia, and S. Kalliadasis, Physics-informed Bayesian inference of external potentials in classical density-functional theory, *J. Chem. Phys* **159**, 104109 (2023).

[35] R. Pederson, B. Kalita, and K. Burke, Machine learning and density functional theory, *Nat. Rev. Phys* **4**, 357 (2022).

[36] F. Sammüller, S. Hermann, D. de las Heras, and M. Schmidt, Neural functional theory for inhomogeneous fluids: Fundamentals and applications, *Proc. Natl. Acad. Sci. U.S.A* **120**, e2312484120 (2023).

[37] F. Sammüller, M. Schmidt, and R. Evans, *Neural density functional theory of liquid-gas phase coexistence* (2024), arXiv:2408.15835 [cond-mat.soft].

[38] J. C. Shelley and G. N. Patey, A configuration bias Monte Carlo method for ionic solutions, *J. Chem. Phys* **100**, 8265 (1994).

[39] Q. Yan and J. J. de Pablo, Hyper-parallel tempering Monte Carlo: Application to the Lennard-Jones fluid and the restricted primitive model, *J. Chem. Phys* **111**, 9509 (1999).

[40] F. Moučka, M. Lísal, J. Škvor, J. Jirsák, I. Nezbeda, and W. R. Smith, Molecular simulation of aqueous electrolyte solubility. 2. Osmotic ensemble Monte Carlo methodology for free energy and solubility calculations and application to NaCl, *J. Phys. Chem. B* **115**, 7849 (2011).

[41] F. Moučka, D. Bratko, and A. Luzar, Electrolyte pore/solution partitioning by expanded grand canonical ensemble Monte Carlo simulation, *J. Chem. Phys* **142**, 124705 (2015).

[42] J. Kim, L. Belloni, and B. Rotenberg, Grand-canonical molecular dynamics simulations powered by a hybrid 4D nonequilibrium MD/MC method: Implementation in LAMMPS and applications to electrolyte solutions, *J. Chem. Phys* **159**, 144802 (2023).

[43] J. M. Rodgers and J. D. Weeks, Local molecular field theory for the treatment of electrostatics, *J. Phys. Condens. Matter* **20**, 494206 (2008).

[44] J. D. Weeks, K. Katsov, and K. Vollmayr, Roles of repulsive and attractive forces in determining the structure of nonuniform liquids: Generalized mean field theory, *Phys. Rev. Lett.* **81**, 4400 (1998).

[45] J. M. Rodgers, C. Kaur, Y.-G. Chen, and J. D. Weeks, Attraction between like-charged walls: Short-ranged simulations using local molecular field theory, *Phys. Rev. Lett.* **97**, 097801 (2006).

[46] Y.-g. Chen, C. Kaur, and J. D. Weeks, Connecting systems with short and long ranged interactions: Local molecular field theory for ionic fluids, *J. Phys. Chem. B* **108**, 19874 (2004).

[47] R. C. Remsing, S. Liu, and J. D. Weeks, Long-ranged contributions to solvation free energies from theory and short-ranged models, *Proc. Natl. Acad. Sci. U.S.A* **113**, 2819 (2016).

[48] A. J. Archer and R. Evans, Relationship between local molecular field theory and density functional theory for non-uniform liquids, *J. Chem. Phys* **138**, 014502 (2013).

[49] See Supplemental Material at URL-will-be-inserted-by-publisher.

[50] The critical temperature of the RPM is  $T_c^* = 0.0492$  (from Ref. 39).

[51] D. Frenkel and B. Smit, *Understanding Molecular Simulation: From Algorithms to Applications* (Elsevier Science, 2023).

[52] F. Sammüller and M. Schmidt, Neural density functionals: Local learning and pair-correlation matching, *Phys. Rev. E* **110**, L032601 (2024).

[53] L. S. Ornstein and F. Zernike, Accidental deviations of density and opalescence at the critical point of a single substance, *Proc. R. Neth. Acad. Arts Sci.* **17**, 793 (1914).

[54] R. J. Baxter, Ornstein-Zernike relation and Percus-Yevick approximation for fluid mixtures, *J. Chem. Phys* **52**, 4559 (2003).

[55] S. J. Cox, Dielectric response with short-ranged electrostatics, *Proc. Natl. Acad. Sci. U.S.A* **117**, 19746 (2020).

[56] F. H. Stillinger and R. Lovett, General restriction on the distribution of ions in electrolytes, *J. Chem. Phys* **49**, 1991 (1968).

[57] F. H. Stillinger and R. Lovett, Ion-pair theory of concentrated electrolytes. I. Basic concepts, *J. Chem. Phys* **48**, 3858 (1968).

[58] The number densities also have a functional dependence on the non-electrostatic contribution to the external potential.

As this is the same for both the full and mimic systems, i.e.  $\{V_\nu\} = \{V_{\nu,R}\}$ , we do not indicate this functional dependence explicitly in Eq. 7.

[59] J. M. Rodgers and J. D. Weeks, Accurate thermodynamics for short-ranged truncations of Coulomb interactions in site-site molecular models, *J. Chem. Phys.* **131**, 244108 (2009).

[60] N. F. Carnahan and K. E. Starling, Equation of state for nonattracting rigid spheres, *J. Chem. Phys.* **51**, 635 (1969).

[61] J. L. Lebowitz and J. K. Percus, Mean spherical model for lattice gases with extended hard cores and continuum fluids, *Phys. Rev.* **144**, 251 (1966).

[62] L. Blum, Mean spherical model for asymmetric electrolytes, *Mol. Phys.* **30**, 1529 (1975).

[63] Y.-G. Chen and J. D. Weeks, Local molecular field theory for effective attractions between like charged objects in systems with strong Coulomb interactions, *Proc. Natl. Acad. Sci. U.S.A.* **103**, 7560 (2006).

[64] M. Stengel, N. A. Spaldin, and D. Vanderbilt, Electric displacement as the fundamental variable in electronic-structure calculations, *Nat. Phys.* **5**, 304 (2009).

[65] C. Zhang and M. Sprik, Computing the dielectric constant of liquid water at constant dielectric displacement, *Phys. Rev. B* **93**, 144201 (2016).

[66] C. Zhang and M. Sprik, Finite field methods for the supercell modeling of charged insulator/electrolyte interfaces, *Phys. Rev. B* **94**, 245309 (2016).

[67] M. Sprik, Finite Maxwell field and electric displacement Hamiltonians derived from a current dependent Lagrangian, *Molecular Physics* **116**, 3114 (2018).

[68] S. J. Cox and M. Sprik, Finite field formalism for bulk electrolyte solutions, *J. Chem. Phys.* **151**, 064506 (2019).

[69] T. Sayer and S. J. Cox, Macroscopic surface charges from microscopic simulations, *J. Chem. Phys.* **153**, 164709 (2020).

[70] C. Zhang, T. Sayer, J. Hutter, and M. Sprik, Modelling electrochemical systems with finite field molecular dynamics, *Journal of Physics: Energy* **2**, 032005 (2020).

[71] D. Henderson and L. Blum, Some exact results and the application of the mean spherical approximation to charged hard spheres near a charged hard wall, *J. Chem. Phys.* **69**, 5441 (1978).

[72] D. Henderson, L. Blum, and J. L. Lebowitz, An exact formula for the contact value of the density profile of a system of charged hard spheres near a charged wall, *J. Electroanal. Chem.* **102**, 315 (1979).

[73] P. A. Martin, Sum rules in charged fluids, *Rev. Mod. Phys.* **60**, 1075 (1988).

[74] This equation for  $\sigma_s$  assumes that the electrolyte is centered in a periodically replicated cell of length  $L$  along the  $z$  direction.

[75] A. Voukadinova, M. Valiskó, and D. Gillespie, Assessing the accuracy of three classical density functional theories of the electrical double layer, *Phys. Rev. E* **98**, 012116 (2018).

[76] D. Gillespie, Restoring the consistency with the contact density theorem of a classical density functional theory of ions at a planar electrical double layer, *Phys. Rev. E* **90**, 052134 (2014).

[77] P. Cats and R. van Roij, The differential capacitance as a probe for the electric double layer structure and the electrolyte bulk composition, *J. Chem. Phys.* **155**, 104702 (2021).

[78] A. T. Bui and S. J. Cox, A classical density functional theory for solvation across length scales, *J. Chem. Phys.* **161**, 104103 (2024).

[79] A. Gao, R. C. Remsing, and J. D. Weeks, Local molecular field theory for Coulomb interactions in aqueous solutions, *J. Phys. Chem. B* **127**, 809 (2023).

[80] J. M. Rodgers and J. D. Weeks, Interplay of local hydrogen-bonding and long-ranged dipolar forces in simulations of confined water, *Proc. Natl. Acad. Sci. U.S.A.* **105**, 19136 (2008).

[81] A. T. Bui and S. J. Cox, ion-cdft, <https://github.com/annatbui/XXXXX> (2024).

[82] A. T. Bui and S. J. Cox, Research data supporting “Learning classical density functionals for ionic fluids”. Zenodo., <https://doi.org/10.5281/zenodo.XXXXX> (2024).

# Supplemental material: Learning classical density functionals for ionic fluids

Anna T. Bui<sup>1</sup> and Stephen J. Cox<sup>2, a)</sup>

<sup>1)</sup>*Yusuf Hamied Department of Chemistry, University of Cambridge, Lensfield Road, Cambridge, CB2 1EW, United Kingdom*

<sup>2)</sup>*Department of Chemistry, Durham University, South Road, Durham, DH1 3LE, United Kingdom*

(Dated: October 4, 2024)

## CONTENTS

<b>S1. Classical density functional theory</b>	S2
<b>S2. Simulations of the short-ranged system</b>	S2
S2.1. GCMC simulations	S3
S2.2. Bulk canonical MD simulations	S3
<b>S3. Simulations of the long-ranged system</b>	S4
S3.1. Bulk GCMC simulations	S4
S3.2. Canonical MD simulations	S4
<b>S4. Connecting the short-ranged and long-ranged systems</b>	S4
S4.1. Structure	S4
S4.2. Liquid–vapor coexistence	S5
S4.3. Energy	S5
S4.4. Chemical potential	S6
S4.5. Pressure	S6
<b>S5. Finite field simulations</b>	S7
<b>S6. Distribution functions</b>	S8
<b>S7. Training one-body direct correlation neural functionals</b>	S10
S7.1. Training data	S10
S7.2. Neural network	S11
S7.3. Training procedure	S11
S7.4. Bulk correlation matching	S13
<b>S8. Electric double layer</b>	S13
<b>References</b>	S15

<sup>a)</sup>Electronic mail: [stephen.j.cox@durham.ac.uk](mailto:stephen.j.cox@durham.ac.uk)

## S1. CLASSICAL DENSITY FUNCTIONAL THEORY

For an  $n$ -component ionic fluid described by the singlet ion densities  $\{\rho_\nu(\mathbf{r})\}$  ( $\nu = 1, 2, \dots, n$ ) with the charge carried by ions of species  $\nu$  being  $q_\nu$ , the grand potential functional is

$$\Omega[\{\rho_\nu\}] = \mathcal{F}_{\text{intr}}[\{\rho_\nu\}] - \sum_\nu \int d\mathbf{r} [\mu_\nu - V_\nu(\mathbf{r}) - q_\nu \phi(\mathbf{r})] \rho_\nu(\mathbf{r}), \quad (\text{S1})$$

where  $\mu_\nu$  is the chemical potential of species  $\nu$ ,  $V_\nu$  contains all non-coulombic contributions to the external potential on species  $\nu$ , and  $\phi$  is the electrostatic potential. The intrinsic Helmholtz free energy functional  $\mathcal{F}_{\text{intr}}$  can be divided exactly into ideal and excess parts

$$\beta \mathcal{F}_{\text{intr}}[\{\rho_\nu\}] = \sum_\nu \int d\mathbf{r} \rho_\nu(\mathbf{r}) [\ln(\Lambda_\nu^3 \rho_\nu(\mathbf{r})) - 1] + \beta \mathcal{F}_{\text{intr}}^{(\text{ex})}[\{\rho_\nu\}], \quad (\text{S2})$$

with  $\beta = (k_B T)^{-1}$ , where  $k_B$  is Boltzmann's constant,  $T$  is the temperature and  $\Lambda_\nu$  is the de Broglie thermal wavelength of species  $\nu$ . The intrinsic excess free energy functional  $\mathcal{F}_{\text{intr}}^{(\text{ex})}$  acts as a generating functional for the one-body direct correlation function of each species  $\nu$ :

$$c_\nu^{(1)}(\mathbf{r}, [\{\rho_\nu\}]) = -\frac{\beta \delta \mathcal{F}_{\text{intr}}^{(\text{ex})}[\{\rho_\nu\}]}{\delta \rho_\nu(\mathbf{r})}. \quad (\text{S3})$$

The variational principle states that the equilibrium ion densities minimise  $\Omega$ , so the Euler–Lagrange equation for each species  $\nu$  is given as

$$\rho_\nu(\mathbf{r}) = \Lambda_\nu^{-3} \exp \left( -\beta V_\nu(\mathbf{r}) - \beta q_\nu \phi(\mathbf{r}) + \beta \mu_\nu + c_\nu^{(1)}(\mathbf{r}; [\{\rho_\nu\}]) \right). \quad (\text{S4})$$

Upon rearrangement, we can write the relationship for learning the one-body correlation functions

$$c_\nu^{(1)}(\mathbf{r}) = \ln(\Lambda_\nu^3 \rho_\nu(\mathbf{r})) + \beta V_\nu(\mathbf{r}) + \beta q_\nu \phi(\mathbf{r}) - \beta \mu_\nu. \quad (\text{S5})$$

## S2. SIMULATIONS OF THE SHORT-RANGED SYSTEM

The full system we considered is the restricted primitive model (RPM) in which the solvent is treated as a dielectric continuum with dielectric constant  $\epsilon$ , and the ions are modeled as hard spheres of two species (cations and anions) that are characterized by equal diameter  $\sigma$  and opposite charges  $q_+ = -q_-$ . The pair potentials of the RPM are defined by

$$u_{ij}(r) = \begin{cases} \infty & r \leq \sigma \\ \frac{q_i q_j}{\epsilon} \frac{1}{r} & r > \sigma. \end{cases} \quad (\text{S6})$$

Throughout, we adopt the Gaussian unit system for electrostatics in which  $4\pi\epsilon_0 = 1$  where  $\epsilon_0$  is the permittivity of free space. The short-ranged mimic system has pair potentials

$$u_{ij,R}(r) = \begin{cases} \infty & r \leq \sigma \\ \frac{q_i q_j}{\epsilon} \frac{\text{erfc}(\kappa r)}{r} & \sigma < r \leq r_c \\ 0 & r > r_c, \end{cases} \quad (\text{S7})$$

where  $\kappa^{-1} = 1.81\sigma$  and  $r_c = 3.6\sigma$ . It is also convenient to introduce a reduced unit system, in which the unit of energy is  $|q_\pm|^2/\epsilon\sigma$ . Therefore, the reduced temperature is given as

$$T^* = \frac{\epsilon \sigma k_B T}{|q_\pm|^2}. \quad (\text{S8})$$

In the article, we focus on the RPM at  $T^* = 0.066$  under supercritical condition. In the main paper, we report quantities in their reduced units. Here in the SM, to stay in line with how the simulations are performed in practice, we will report quantities in “real” units and we employed  $\sigma = 2.76 \text{ \AA}$ ,  $q_- = -q_+ = e$  where  $e$  is the elementary charge and  $\epsilon = 1$ , which corresponds to molten NaCl<sup>1</sup> at  $T = 4000 \text{ K}$ .

### S2.1. GCMC simulations

For the short-ranged systems, we performed GCMC simulations with our own code <https://github.com/annatbui/GCMC>. Insertion and deletion moves were performed separately for each ionic species, i.e.,  $\mu_{R,+}$  and  $\mu_{R,-}$  were controlled independently. Cubic simulation boxes of length  $L = 24 \text{ \AA}$  with periodic boundary conditions were used. Each system was equilibrated for at least  $1 \times 10^5$  MC steps. In each MC move, there are five possibilities with the following transition probabilities from state  $i$  to state  $j$ ,  $p_j/p_i$ :

(a) Displacement of an ion of species  $\nu$

$$\frac{p_j}{p_i} = \exp(-\beta \Delta U_{ji}), \quad (\text{S9})$$

(b) Insertion of an ion of species  $\nu$

$$\frac{p_j}{p_i} = \frac{V}{(N_\nu + 1) \Lambda_\nu^3} \exp(-\beta \Delta U_{ji} + \beta \mu_{R,\nu}), \quad (\text{S10})$$

(c) Deletion of an ion of species  $\nu$

$$\frac{p_j}{p_i} = \frac{N_\nu \Lambda_\nu^3}{V} \exp(-\beta \Delta U_{ji} - \beta \mu_{R,\nu}), \quad (\text{S11})$$

(d) Mutation of an ion of species  $\nu$  to an ion of species  $\lambda$

$$\frac{p_j}{p_i} = \frac{N_\nu \Lambda_\nu^3}{(N_\lambda + 1) \Lambda_\lambda^3} \exp(-\beta \Delta U_{ji} - \beta \mu_{R,\nu} + \beta \mu_{R,\lambda}), \quad (\text{S12})$$

(e) Swap position of an ion of species  $\nu$  with an ion of species  $\lambda$

$$\frac{p_j}{p_i} = \exp(-\beta \Delta U_{ji}), \quad (\text{S13})$$

where  $N_\nu$  denotes the number of ions of species  $\nu$ ,  $V$  is the volume of the simulation box and  $\Delta U_{ji}$  is the change in potential energy between state  $i$  and state  $j$ , including any contribution from external potentials. In all cases, a trial move was accepted with probability  $\min(1, p_j/p_i)$  by drawing a random number uniformly in the interval  $[0, 1)$ .

For each simulation, around  $1 \times 10^9$  MC steps were attempted.

### S2.2. Bulk canonical MD simulations

MD simulations of the short-ranged system were performed with the LAMMPS simulation package.<sup>2</sup> Source code to implement the pair potential with short-ranged electrostatics can be accessed at <https://github.com/uccasco/LMFT>.<sup>3</sup> Cubic simulation boxes with periodic boundary conditions were used. The bulk systems contained 2000 ion pairs, with the length of the box adjusted to yield the desired bulk densities. Dynamics were propagated using the velocity Verlet algorithm with a time-step of 1 fs. The temperature was maintained using a Langevin thermostat.<sup>4</sup> The system was equilibrated for 50 ps and production runs were performed for at least 2 ns in the NVT ensemble.

To describe the hard-core part of the pair interaction in MD simulations, as done in Refs. 5 and 6, we use the pseudo hard-sphere potential

$$u_{\text{pHS}}(r) = \begin{cases} 50 \left(\frac{50}{49}\right)^{49} \varepsilon \left[ \left(\frac{\sigma}{r}\right)^{50} - \left(\frac{\sigma}{r}\right)^{49} \right] + \varepsilon & r \leq \left(\frac{50}{49}\right) \sigma \\ 0 & r > \left(\frac{50}{49}\right) \sigma, \end{cases} \quad (\text{S14})$$

at  $k_B T / \varepsilon = 1.5$ , which was found to reproduce structural and thermodynamic data of hard-spheres.<sup>7</sup>

### S3. SIMULATIONS OF THE LONG-RANGED SYSTEM

#### S3.1. Bulk GCMC simulations

For the full long-ranged system, we performed GCMC simulations with DL\_MONTE.<sup>8</sup> Long-ranged electrostatics were treated with Ewald summation.<sup>9,10</sup> As insertion and deletion moves can only be done with pairs of ion effectively, we controlled  $\mu_{\text{pair}} = \mu_+ + \mu_-$ . Cubic simulation boxes with periodic boundary conditions were used. The system was equilibrated for  $1 \times 10^4$  MC steps and  $1 \times 10^8$  MC steps were attempted in the production run.

#### S3.2. Canonical MD simulations

MD simulations of the long-ranged system were performed with the LAMMPS simulation package.<sup>2</sup> Cubic simulation boxes with periodic boundary conditions were used. The bulk systems contained 2000 ion pairs, with the length of the box adjusted to yield the desired bulk densities. Dynamics were propagated using the velocity Verlet algorithm with a time-step of 1 fs. The temperature was maintained using a Langevin thermostat.<sup>4</sup> The system was equilibrated for 50 ps and production runs were performed for at least 2 ns in the NVT ensemble.

Long-ranged electrostatic interactions were evaluated using particle-particle particle-mesh Ewald summation<sup>11</sup> (using a 1 nm cut off in real space) such that the RMSE in the forces was a factor of  $10^5$  smaller than the force between two unit charges separated by a distance of 0.1 nm.<sup>12</sup>

### S4. CONNECTING THE SHORT-RANGED AND LONG-RANGED SYSTEMS

#### S4.1. Structure

The pair potentials for the long-ranged and mimic short-ranged systems are described in Eq. S6 and Eq. S7 and plotted in Fig. S1(a). With  $\kappa^{-1}$  chosen to be large enough, the mimic system can faithfully capture the short-ranged local structure of the full system in the bulk, reflected in the radial distribution functions in Fig. S1(b). For the bulk structure, discrepancies between the mimic and full system would only appear at longer wavelength, as shown in the structure factors in the main paper.

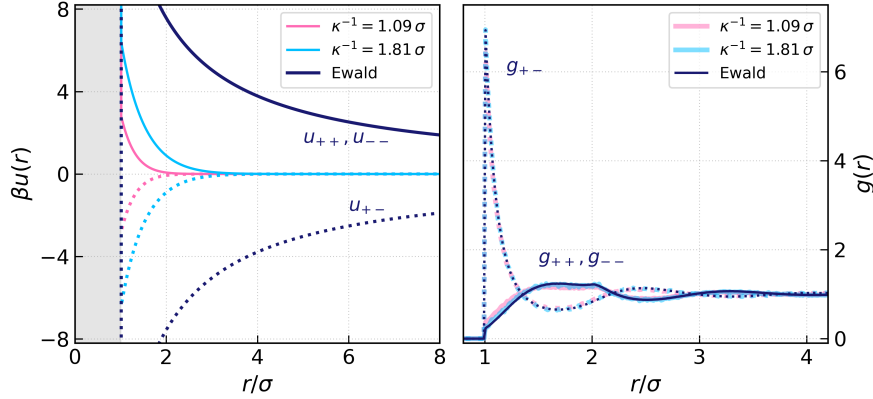


**Figure S1: Structure of the short-ranged and long-ranged RPM.** (a) The pair potential and (b) radial distribution function of a bulk fluid at the same density  $\rho_+ = \rho_- = 0.315 \sigma^{-3}$  obtained from GCMC simulations. The cation–cation and anion–anion functions are shown in solid lines while cation–anion functions are in dotted lines.

#### S4.2. Liquid–vapor coexistence

For the long-ranged RPM, the liquid–vapor binodal curve has been determined<sup>13</sup> with the critical temperature  $T_c^* = 0.0492$ . Short-ranged fluids are expected to have a lower critical temperature than their long-ranged counterpart.<sup>14</sup> Indeed, we verified this by constructing the binodal curve for two short-ranged mimic systems from GCMC simulations, as shown in Fig. S2(a). In this work, we focus on the isothermal behavior at  $T^* = 0.066$ , which is supercritical for both the full RPM and the mimic system.

#### S4.3. Energy

In Ref. 15, an analytical correction for the Coulombic energy between the long-ranged and short-ranged bulk systems based on the Stillinger–Lovett moment conditions is derived. For a binary salt, this long-range correction reduces to

$$\Delta U \equiv U - U_R = -\frac{V}{\kappa^{-1}\sqrt{\pi}} (\rho_+ q_+^2 + \rho_- q_-^2) + \frac{1}{\kappa^{-3}\sqrt{\pi}} \frac{V}{2\pi\beta}, \quad (\text{S15})$$

where  $V$  is the volume of the system. As seen in Fig. S2, for mimic systems with  $\kappa^{-1} > \sigma$ , the total potential energy with this correction reproduces the energy of the full system (calculated with Ewald sums) well.

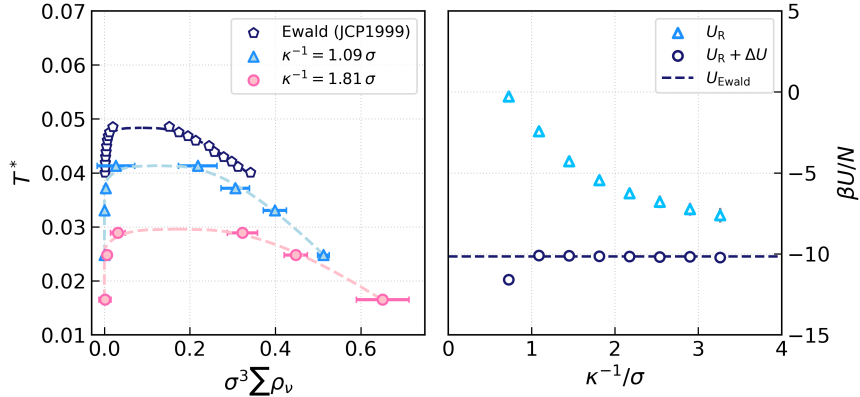


**Figure S2: Phase diagram and potential energy long-range correction of the RPM.** (a) The liquid–vapor coexistence curve of the long-ranged system is from Ref. 13, while those of the short-ranged mimic systems are determined in this work. (b) The total potential energy of the mimic short-ranged system at various  $\kappa^{-1}$  without (triangles) and with the long-range correction (circles) for the bulk system at  $\rho_{R,+} = \rho_{R,-} = 0.263\sigma^{-3}$ . The energy determined from Ewald summation is indicated by the horizontal dashed line.

#### S4.4. Chemical potential

The change in internal energy of the bulk system is given as

$$dU = TdS + \mu_+ dN_+ + \mu_- dN_- - PdV, \quad (\text{S16})$$

where  $S$  is the entropy,  $N_+$  is the number of cations,  $N_-$  is the number of anions and  $P$  is the pressure. The chemical potentials of the anion  $\mu_-$  and cation  $\mu_+$  can be expressed thermodynamically as

$$\begin{aligned} \mu_- &= \left( \frac{\partial U}{\partial N_-} \right)_{\mu_+, V, T} - T \left( \frac{\partial S}{\partial N_-} \right)_{\mu_+, V, T}, \\ \mu_+ &= \left( \frac{\partial U}{\partial N_+} \right)_{\mu_-, V, T} - T \left( \frac{\partial S}{\partial N_+} \right)_{\mu_-, V, T}. \end{aligned} \quad (\text{S17})$$

Since the mimic system is constructed to capture the local order and structural variations that are expected to dominate the entropy, we approximate  $S \approx S_R$ , giving:

$$\begin{aligned} \Delta\mu_- \equiv \mu_- - \mu_{R,-} &= \left( \frac{\partial \Delta U}{\partial N_-} \right)_{\mu_-, V, T} = -\frac{q_+^2}{\kappa^{-1} \sqrt{\pi}}, \\ \Delta\mu_+ \equiv \mu_+ - \mu_{R,+} &= \left( \frac{\partial \Delta U}{\partial N_+} \right)_{\mu_-, V, T} = -\frac{q_-^2}{\kappa^{-1} \sqrt{\pi}}. \end{aligned} \quad (\text{S18})$$

For a range of  $\kappa^{-1}$ , we find the chemical potentials that gives a bulk fluid of density  $\rho_{R,+} = \rho_{R,-} = 0.263\sigma^{-3}$  by running GCMC simulations with various  $\mu_{R,-} = \mu_{R,+}$ . As shown in Fig. S3(a), for  $\kappa^{-1} \gtrsim \sigma$ , the corrected chemical potentials of the mimic system agree well with that of the full system. The long-ranged GCMC simulations were done with insertions and deletions of cation-ion pairs so the chemical potential is  $\mu_- = \mu_+ = \mu_{\text{pair}}/2$ .

#### S4.5. Pressure

The pressure can be expressed thermodynamically as

$$P = T \left( \frac{\partial S}{\partial V} \right)_{N_+, N_-, T} - \left( \frac{\partial U}{\partial V} \right)_{N_+, N_-, T}. \quad (\text{S19})$$

Again,  $S \approx S_R$ , leaving the correction for the bulk pressure, consistent with Ref. 15, as

$$\Delta P \equiv P - P_R = - \left( \frac{\partial \Delta U}{\partial V} \right)_{N_+, N_-, T} = - \frac{1}{2\pi^{3/2} \kappa^{-3} \beta}. \quad (S20)$$

The pressure obtained from simulations of the mimic systems is shown in Fig. S3(b). The analytical pressure correction brings the result closer to the pressure of the long-ranged system. For dense systems, its contribution is relatively small.

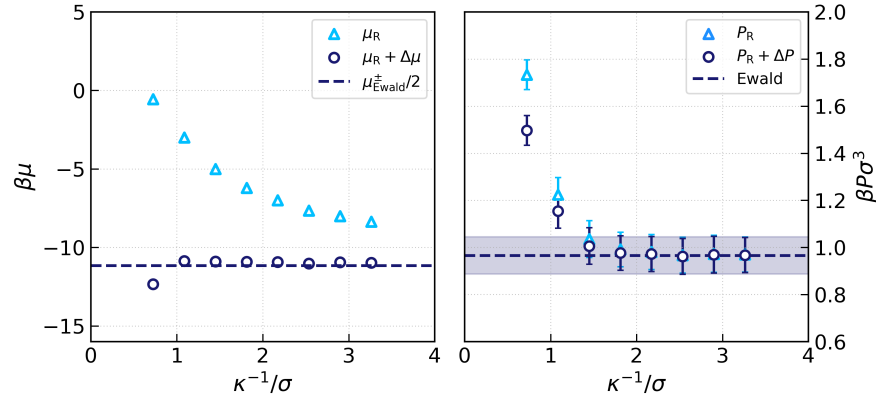


**Figure S3: Long-range corrections for the chemical potential and pressure for the RPM.** (a) The chemical potential for an ion and (b) the pressure of the mimic short-ranged system at at various  $\kappa^{-1}$  without (triangles) and with the long-range correction (circles) for the bulk system at  $\rho_{R,+} = \rho_{R,-} = 0.263 \sigma^{-3}$ . The results for the full system (determined with Ewald sums) are indicated by the horizontal dashed lines, with uncertainty in the pressure indicated by the shaded region.

## S5. FINITE FIELD SIMULATIONS

The Hamiltonian of the system under an imposed uniform  $\mathbf{E}$  field is given as

$$\mathcal{H}_E(\mathbf{r}^N, \mathbf{p}^N) = \mathcal{H}_{\text{PBC}}(\mathbf{r}^N, \mathbf{p}^N) - V\mathbf{E} \cdot \mathbf{P}(\mathbf{r}^N), \quad (S21)$$

where  $\mathcal{H}_{\text{PBC}}$  denotes the Hamiltonian of the periodic system computed using standard Ewald summation techniques and  $\mathbf{P}$  denotes the total polarization formally defined as the time integral of the current

$$\mathbf{P}(\mathbf{r}^N) = \frac{1}{V} \sum_i q_i \mathbf{r}_i. \quad (S22)$$

In our simulations, we use an “electrolyte centered cell” such that the above amounts to a straightforward calculation of the total dipole moment of the simulation cell.<sup>16-18</sup> In MD simulations, this amounts to adding a force  $\mathbf{f}_i = q_i \mathbf{E}$  to each ion  $i$  in the simulation.

The finite field Hamiltonian for the system under constant displacement field  $\mathbf{D}$  is

$$\mathcal{H}_D(\mathbf{r}^N, \mathbf{p}^N) = \mathcal{H}_{\text{PBC}}(\mathbf{r}^N, \mathbf{p}^N) + \frac{V}{8\pi} [\mathbf{D} - 4\pi\mathbf{P}(\mathbf{r}^N)]^2. \quad (S23)$$

The displacement field is related to the electric field through

$$\mathbf{D} = \mathbf{E} + 4\pi\mathbf{P}. \quad (S24)$$

In MD simulations, this amounts to adding a field-dependent force to each ion  $\mathbf{f}_i = q_i(\mathbf{D} - 4\pi\mathbf{P})$ .

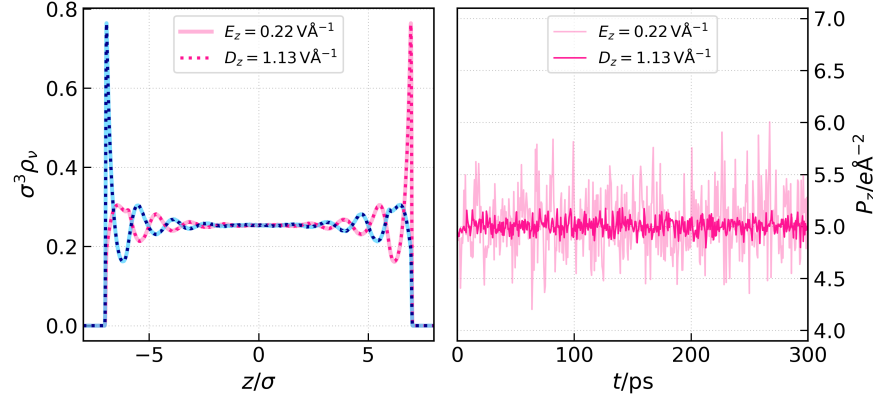


**Figure S4: Finite field simulations of the RPM confined between two oppositely charged walls.** (a) Ion density profiles obtained are identical under a constant electric field  $E_z = 0.22 \text{ V} \text{ \AA}^{-1}$  or under a constant displacement field  $D_z = 1.13 \text{ V} \text{ \AA}^{-1}$ . (b) The polarization  $P_z$  in the two simulations are on average the same, with smaller fluctuations under constant  $D_z$ .

## S6. DISTRIBUTION FUNCTIONS

We denote the 3D spatial Fourier transform of function  $f(\mathbf{r})$  as

$$\hat{f}(\mathbf{k}) = \int d\mathbf{r} f(\mathbf{r}) \exp(-i\mathbf{k} \cdot \mathbf{r}), \quad (\text{S25})$$

and the inverse Fourier transform of  $\hat{f}(\mathbf{k})$  as

$$f(\mathbf{r}) = \frac{1}{(2\pi)^3} \int d\mathbf{k} \hat{f}(\mathbf{k}) \exp(i\mathbf{k} \cdot \mathbf{r}). \quad (\text{S26})$$

For a radially symmetric function  $f(r)$ , the corresponding expressions become

$$\hat{f}(k) = \frac{4\pi}{k} \int_0^\infty dr r f(r) \sin(kr), \quad (\text{S27})$$

and

$$f(r) = \frac{1}{2\pi^2 r} \int_0^\infty dk k \hat{f}(k) \sin(kr). \quad (\text{S28})$$

The planar projection of a radially symmetric function  $f(r)$  is

$$\bar{f}(z) = \int dx \int dy f(r = \sqrt{x^2 + y^2 + z^2}) = 2\pi \int_z^\infty dr r f(r), \quad (\text{S29})$$

and the inverse transformation is

$$f(r) = -\frac{1}{2\pi r} \frac{\partial \bar{f}(z)}{\partial z} \Big|_{z=r}. \quad (\text{S30})$$

For a bulk mixture containing  $N_\nu$  of species  $\nu$ , we extracted the radial distribution functions

$$g_{\nu\lambda}(r) = \frac{\rho_{\text{tot}}}{\rho_\nu \rho_\lambda} \left\langle \frac{1}{N} \sum_i^{N_\nu} \sum_j^{N_\lambda} \delta(r - |\mathbf{r}_i - \mathbf{r}_j|) \right\rangle, \quad (\text{S31})$$

where  $\rho_{\text{tot}} = \sum_\nu \rho_\nu = \sum_\nu N_\nu/V$ , by generating a histogram of intermolecular distances and appropriate

normalization. The corresponding total correlation functions are therefore

$$h_{\nu\lambda}(r) = g_{\nu\lambda}(r) - 1. \quad (\text{S32})$$

The high-wavevector part of the partial structure factors are computed from

$$S_{\nu\lambda}(k) = \frac{\rho_\nu}{\rho_{\text{tot}}} \delta_{\nu\lambda} + \frac{\rho_\nu \rho_\lambda}{\rho_{\text{tot}}} \hat{h}_{\nu\lambda}(k). \quad (\text{S33})$$

In the low-wavevector limit, we also calculate the structure factor directly from the simulation trajectories using<sup>19</sup>

$$\begin{aligned} S_{\nu\lambda}(k) &= \left\langle \frac{1}{N} \sum_i^{N_\nu} \sum_j^{N_\lambda} \exp[-i\mathbf{k} \cdot (\mathbf{r}_i - \mathbf{r}_j)] \right\rangle \\ &= \frac{1}{N} \left\langle \left[ \sum_i^{N_\nu} \sin(\mathbf{k} \cdot \mathbf{r}_i) \right] \left[ \sum_i^{N_\lambda} \sin(\mathbf{k} \cdot \mathbf{r}_i) \right] + \left[ \sum_i^{N_\nu} \cos(\mathbf{k} \cdot \mathbf{r}_i) \right] \left[ \sum_i^{N_\lambda} \cos(\mathbf{k} \cdot \mathbf{r}_i) \right] \right\rangle. \end{aligned} \quad (\text{S34})$$

The Ornstein–Zernike equation that relates the two-body direct correlation functions to the total correlation function for a homogeneous mixture is

$$h_{\nu\lambda}(r) = c_{\nu\lambda}^{(2)}(r) + \sum_\gamma^n \rho_\gamma \int d\mathbf{r}' c_{\nu\gamma}^{(2)}(|\mathbf{r} - \mathbf{r}'|) h_{\gamma\lambda}(|\mathbf{r}'|). \quad (\text{S35})$$

It is convenient to define two matrices with components<sup>20</sup>

$$\hat{H}_{\nu\lambda}(k) = (\rho_\nu \rho_\lambda)^{1/2} \hat{h}_{\nu\lambda}(k), \quad (\text{S36})$$

$$\hat{C}_{\nu\lambda}(k) = (\rho_\nu \rho_\lambda)^{1/2} \hat{c}_{\nu\lambda}^{(2)}(k), \quad (\text{S37})$$

allowing the Ornstein–Zernike equation to be recast in a matrix form

$$\hat{H}(k) = \hat{C}(k) + \hat{C}(k) \hat{H}(k). \quad (\text{S38})$$

Upon rearrangement,

$$\hat{C}(k) = \mathbf{I} - [\mathbf{I} + \hat{H}(k)]^{-1}, \quad (\text{S39})$$

where  $\mathbf{I}$  is the identity matrix.

To obtain the planar bulk two-body direct correlation functions  $\bar{c}_{R,\nu\lambda}^{(2)}(z; \{\rho_b\})$ , where  $\rho_b = \rho_{R,\pm}$  denotes the bulk ionic density, from simulations for bulk correlation matching, we calculate in order:

- $S_{R,\nu\lambda}(k; \{\rho_b\})$  at the low-wavevector end ( $k\sigma < 5$ ) directly via Eq. S34,
- $g_{R,\nu\lambda}(r; \{\rho_b\})$  by generating histograms of interatomic distances via Eq. S31,
- $h_{R,\nu\lambda}(r; \{\rho_b\})$  via Eq. S32,
- $\hat{h}_{R,\nu\lambda}(k; \{\rho_b\})$  at the low-wavevector end through  $S_{R,\nu\lambda}(k; \{\rho_b\})$  via Eq. S33 and at the high-wavevector end via the radial Fourier transform, Eq. S27, of  $h_{R,\nu\lambda}(r; \{\rho_b\})$ ,
- $\hat{H}_{R,\nu\lambda}(k; \{\rho_b\})$  via Eq. S36,
- $\hat{C}_{R,\nu\lambda}(k; \{\rho_b\})$  by solving the matrix equation Eq. S39,
- $\hat{c}_{R,\nu\lambda}^{(2)}(k; \{\rho_b\})$  via Eq. S37,
- $c_{R,\nu\lambda}^{(2)}(r; \{\rho_b\})$  via the inverse radial Fourier transform, Eq. S28, of  $\hat{c}_{R,\nu\lambda}^{(2)}(k; \{\rho_b\})$ ,
- $\bar{c}_{R,\nu\lambda}^{(2)}(z; \{\rho_b\})$  via the planar projection, Eq. S29, of  $c_{R,\nu\lambda}^{(2)}(r; \{\rho_b\})$ .

Some of these functions are shown representatively in Fig. S5.

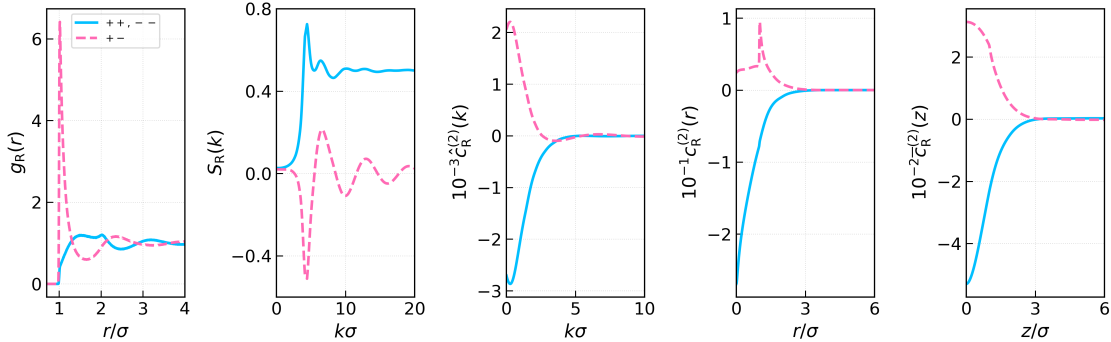


**Figure S5: Distribution functions.** For a short-ranged mimic bulk system at  $\rho_{R,+} = \rho_{R,-} = 0.315 \sigma^{-3}$ , we show the (a) radial distribution functions, (b) partial structure factors, (c) two-body direct correlation functions in reciprocal space, (d) in real space and (e) their planar projections.

## S7. TRAINING ONE-BODY DIRECT CORRELATION NEURAL FUNCTIONALS

### S7.1. Training data

Following Ref. 21, we employ randomized simulation conditions by generating external potentials of the form

$$V_\nu(z) = \sum_{n=1}^4 A_n \sin\left(\frac{2\pi n z}{L_z} + \theta_n\right) + \sum_n B_n^{\text{lin}}(z), \quad (\text{S40})$$

where  $A_n$  and  $\theta_n$  are randomly selected Fourier coefficients and phases, respectively, and  $L_z$  is the simulation box length in the  $z$  direction. The phases  $\theta_n$  are chosen uniformly in the interval  $[0, 2\pi]$ , and values of  $A_n$  are drawn from a normal distribution with zero mean and a variance of  $0.06 (k_B T)^2$ . Cubic simulation boxes with  $L_z = 24 \text{ \AA}$  with periodic boundary conditions were used. The second summation denotes up to four piece-wise linear functions

$$B_n^{\text{lin}}(z) = \begin{cases} V_1 + \frac{V_2 - V_1}{z_2 - z_1}(z - z_1) & z_1 < z < z_2 \\ 0 & \text{otherwise,} \end{cases} \quad (\text{S41})$$

while  $0 < z_1 < z_2 < L_z$ . The locations  $z_1$  and  $z_2$  are distributed uniformly while  $V_1$  and  $V_2$  follow from an unbiased normal distribution with variance of  $(k_B T)^2$ . Similarly, the external electrostatic potential used is also randomized with an analogous form

$$\phi(z) = \sum_{n=1}^4 A_n^q \sin\left(\frac{2\pi n z}{L_z} + \theta_n^q\right) + \sum_n B_n^{\text{lin},q}(z). \quad (\text{S42})$$

For a subset of simulations, we explicitly impose planar hard walls by setting  $V_\nu(z) = \infty$  for  $z < z_w$  and  $z > L_z - z_w$  with  $z_w = 2 \text{ \AA}$ . The chemical potential is randomly chosen in the range  $\beta\mu_{R,\nu} \in [-10.5, -4.0]$ . The thermal wavelengths were set to  $\Lambda_\nu = 1 \text{ \AA}$ .

In total, 2400 GCMC simulations were used including cases with only non-Coulombic external potentials such that  $\phi_R(z) = 0$ , cases with only electrostatic external potentials such that  $V_{R,+}(z) = V_{R,-}(z) = 0$ , symmetric cases where  $V_{R,+}(z) = V_{R,-}(z)$  and  $\mu_{R,+} = \mu_{R,-}$  and asymmetric cases.

For each simulation, the ion density profiles  $\rho_{R,+}(z)$  and  $\rho_{R,-}(z)$  were sampled with a grid-spacing  $\Delta z =$

0.03 Å. The one-body direct correlation profiles are calculated from

$$\begin{aligned} c_{R,-}^{(1)}(z; [\rho_{R,-}]) &= \ln(\Lambda_{-}^3 \rho_{R,-}(z)) + \beta V_{R,-}(z) + \beta q_{-} \phi_{R,-}(z) - \beta \mu_{R,-}, \\ c_{R,+}^{(1)}(z; [\rho_{R,+}]) &= \ln(\Lambda_{+}^3 \rho_{R,+}(z)) + \beta V_{R,+}(z) + \beta q_{+} \phi_{R,+}(z) - \beta \mu_{R,+}. \end{aligned} \quad (S43)$$

### S7.2. Neural network

We used two neural networks to represent the one-body direct correlation functionals, one for  $c_{R,-}^{(1)}$  and one for  $c_{R,+}^{(1)}$ . The machine learning routine was implemented in Keras/Tensorflow with the standard Adam optimizer.<sup>22</sup> The architecture of the models is shown in Fig. S6. The input layers take in both ion density profiles,  $\rho_{R,+}(z)$  and  $\rho_{R,-}(z)$ , in a window of size 10 Å around the location of interest. Three fully-connected hidden layers with 512 nodes and softplus activation functions then follow, finally resulting in a single scalar value  $c_{R,-}^{(1)}(z)$  or  $c_{R,+}^{(1)}(z)$  at position  $z$ . We note that there are also other possible approaches proposed for learning the short-ranged correlations.<sup>23,24</sup>

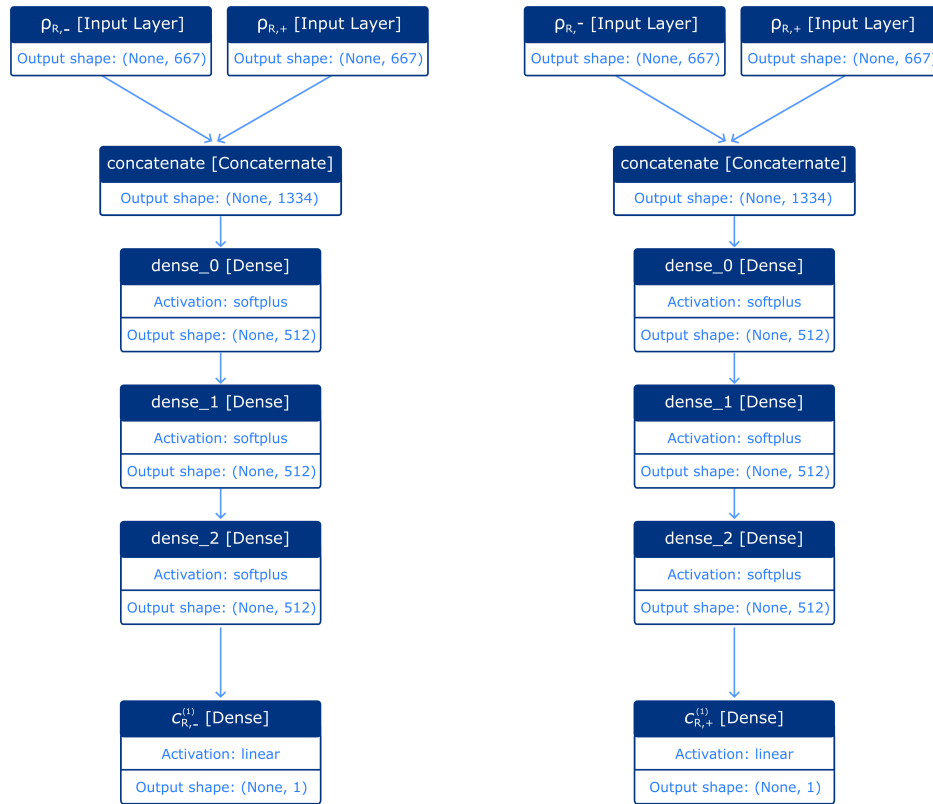


**Figure S6: Architecture of the neural networks.** Two neural networks are trained to represent the one-body direct correlation functionals one for the anion,  $c_{R,-}^{(1)}(z; [\rho_{R,+}, \rho_{R,-}])$ , and one for the cation,  $c_{R,+}^{(1)}(z; [\rho_{R,+}, \rho_{R,-}])$ . The output shapes indicate the variable batch size (“None”) and the number of nodes for each layer.

### S7.3. Training procedure

For the first generation of training, we separate the 2400 independent simulations into 480 for test set, 480 for validation set and 1440 for training set. Each model was trained for 200 epochs in batches of size 256 and the learning rate was decreased exponentially by 5% per epoch from an initial value of 0.001. This results in a best mean average error of 0.034 over the validation set for each model, which is of the same order as the estimated average noise of the simulation data for the one-body direct correlation functions. Employing this model in cDFT for the full LR system gives the results in Fig. S7(a).

In addition to these GCMC simulations with randomized potentials, we further add to the data set 128 simulations in which the SR mimic system experiences the external potential describing the 9-3 Lennard Jones soft walls at randomized values of the chemical potentials. With the updated dataset, we then separate the independent simulations into 505 for test set, 505 for validation set and 1518 for training set. Following the same training procedure as before, this results in a best mean average error of 0.038 and employing this model in cDFT for the full LR system gives the results in Fig. S7(b).

For the last generation of training, we first perform cDFT for the LR full system under an electric field  $E_z$  to generate 72 different data points. From cDFT, we also obtain the corresponding one-body correlation functions  $c_{R,\nu}^{(1)}$  for the mimic system in the process. Using the resulting number density predicted from cDFT, we perform 72 finite-field MD simulations (see Sec. S6) of the LR system and collect the density profiles  $\rho_\nu = \rho_{R,\nu}$ . These 72 combinations of  $\{\rho_{R,\nu}\}$  and  $c_{R,\nu}^{(1)}$  make up the final extra data to the total dataset, which is split into 508 for test set, 508 for validation set and 1524 for training set. Following the same training procedure as before, the final model results in a best mean average error of 0.032 and employing this model in cDFT for the full LR system gives the results in Fig. S7(c).

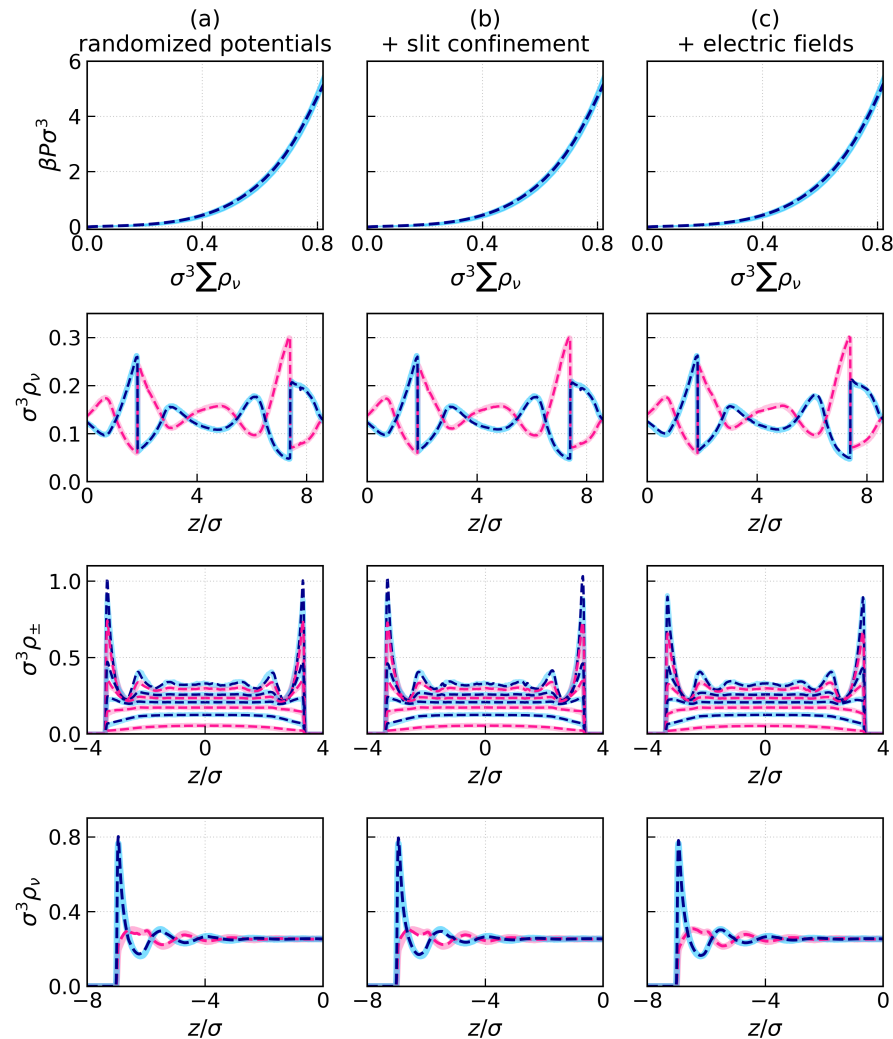


**Figure S7: Performance of cDFT employing different generations of the neural networks for  $\{c_R^{(1)}\}$ .** Results in dashed lines are shown for neural networks trained with (a) randomized potential, (b) with additional slit confinement and (c) with additional electric fields. Overall, good agreement with simulation data (solid lines) is achieved for the equation of state (first row), randomized inhomogeneous profiles (second row), slit confinement (third row) and the electric double layer (final row). The addition of data with electric fields in the final model improves the contact density predictions.

#### S7.4. Bulk correlation matching

To reduce noise in the bulk structure predictions, we also obtained models regularized with bulk two-body direct correlation functions as proposed in Ref. 24. With the bulk simulation of the short-ranged system, we obtain the planar bulk two-body direct correlation functions as described in Section. S6. From the neural network representation of the one-body direct correlation functions, these are the functional derivatives obtainable via automatic differentiation

$$\begin{aligned}\bar{c}_{R,--}^{(2)}(z; \{\rho_b\}) &= \frac{\delta c_{R,-}^{(1)}(0; [\{\rho\}])}{\delta \rho_-(z)} \bigg|_{\{\rho\}=\{\rho_b\}}, \\ \bar{c}_{R,++}^{(2)}(z; \{\rho_b\}) &= \frac{\delta c_{R,+}^{(1)}(0; [\{\rho\}])}{\delta \rho_+(z)} \bigg|_{\{\rho\}=\{\rho_b\}}, \\ \bar{c}_{R,+-}^{(2)}(z; \{\rho_b\}) &= \frac{\delta c_{R,+}^{(1)}(0; [\{\rho\}])}{\delta \rho_-(z)} \bigg|_{\{\rho\}=\{\rho_b\}} = \frac{\delta c_{R,-}^{(1)}(0; [\{\rho\}])}{\delta \rho_+(z)} \bigg|_{\{\rho\}=\{\rho_b\}}.\end{aligned}\quad (S44)$$

To implement bulk correlation matching, we consider the loss functions

$$\begin{aligned}\mathcal{L}_- &= \alpha_{\text{inhom}} \mathcal{L}_-^{\text{inhom}} + \alpha_{\text{pc}} \mathcal{L}_-^{\text{pc}}, \\ \mathcal{L}_+ &= \alpha_{\text{inhom}} \mathcal{L}_+^{\text{inhom}} + \alpha_{\text{pc}} \mathcal{L}_+^{\text{pc}},\end{aligned}\quad (S45)$$

in which the losses from local inhomogeneous one-body learning are given as

$$\begin{aligned}\mathcal{L}_-^{\text{inhom}} &= \sum_i \left[ c_{R,-}^{(1)}(z; \{\rho\}_i) - c_{R,-,\text{sim}}^{(1)}(z; \{\rho\}_i) \right]^2, \\ \mathcal{L}_+^{\text{inhom}} &= \sum_i \left[ c_{R,+}^{(1)}(z; \{\rho\}_i) - c_{R,+,\text{sim}}^{(1)}(z; \{\rho\}_i) \right]^2,\end{aligned}\quad (S46)$$

and the losses from pair-correlation matching are

$$\begin{aligned}\mathcal{L}_-^{\text{pc}} &= \sum_i \left[ \bar{c}_{R,--}^{(2)}(z; \{\rho_b\}_i) - \bar{c}_{R,--,\text{sim}}^{(2)}(z; \{\rho_b\}_i) \right]^2 + \left[ \bar{c}_{R,+-}^{(2)}(z; \{\rho_b\}_i) - \bar{c}_{R,+-,\text{sim}}^{(2)}(z; \{\rho_b\}_i) \right]^2, \\ \mathcal{L}_+^{\text{pc}} &= \sum_i \left[ \bar{c}_{R,++}^{(2)}(z; \{\rho_b\}_i) - \bar{c}_{R,--,\text{sim}}^{(2)}(z; \{\rho_b\}_i) \right]^2 + \left[ \bar{c}_{R,+-}^{(2)}(z; \{\rho_b\}_i) - \bar{c}_{R,+-,\text{sim}}^{(2)}(z; \{\rho_b\}_i) \right]^2.\end{aligned}\quad (S47)$$

The constant factors  $\alpha_{\text{inhom}}$  and  $\alpha_{\text{pc}}$  control the relative influence of inhomogeneous one-body matching and pair-correlation matching by weighting the respective loss terms, for which we employ  $\alpha_{\text{inhom}} = 1$  and  $\alpha_{\text{pc}} = 0.0001$ .

#### S8. ELECTRIC DOUBLE LAYER

The formula for the contact density sum rule for an ionic system at a charged wall is given as<sup>25–27</sup>

$$P = - \sum_{\nu} \int dz \rho_{\nu}(z) \frac{dV_{\nu}(z)}{dz} - \frac{2\pi\sigma_s^2}{\epsilon}, \quad (S48)$$

where  $\sigma_s$  is the surface charge density of the wall. In this section, we will examine the extent to which the cDFT presented in this work obeys Eq. S48. To this end, we focus on systems with the RPM confined in a slit made by two walls with non-electrostatic potential

$$V_{\nu}(z) = \epsilon_{\text{LJ}} \left[ \frac{2}{15} \left( \frac{\sigma_{\text{LJ}}}{z} \right)^9 - \left( \frac{\sigma_{\text{LJ}}}{z} \right)^3 \right] + \epsilon_{\text{LJ}} \left[ \frac{2}{15} \left( \frac{\sigma_{\text{LJ}}}{z_{\min}} \right)^9 - \left( \frac{\sigma_{\text{LJ}}}{z_{\min}} \right)^3 \right], \quad (S49)$$

where  $z_{\min} = \left(\frac{2}{5}\right)^{1/6} \sigma_{\text{LJ}}$ ,  $\sigma_{\text{LJ}} = \sigma$ ,  $\epsilon_{\text{LJ}} = k_{\text{B}}T$  under an electric field  $E_z$ . In the finite field simulations, the two oppositely charged walls are not represented explicitly. Instead, the surface charge is directly determined by the displacement field  $D_z$

$$\sigma_s^{(\text{sim})} = \frac{\langle D_z \rangle}{4\pi} = \frac{E_z}{4\pi} + \langle P_z \rangle. \quad (\text{S50})$$

This approach assumes that the electrolyte screens perfectly, which is reasonable if the region occupied by the electrolyte is thick enough. From the cDFT, we obtain the surface charge by integrating the equilibrium charge densities:

$$\sigma_s^{(\text{cDFT})} = - \int_0^{L_z/2} dz \sum_{\nu} q_{\nu} \rho_{\nu}(z). \quad (\text{S51})$$

We obtained the equilibrium density profiles from cDFT and simulations for the RPM at  $\beta\mu_- = \beta\mu_+ \in [-13.5, -8.5]$  under  $E_z \in [0.0, 0.26] \text{ V \AA}^{-1}$ , a subset of which are shown in Fig. S8(a). The cDFT performs the best for density range  $\sigma^3 \rho_{\pm} \in [0.1, 0.4]$ , as expected since the training data for  $c_R^{(1)}$  focuses on this density region. Higher accuracy for lower and higher density would likely be achieved by extending the training data further. In Fig. S8(b), we verified that  $\sigma_s^{(\text{cDFT})}$  is in agreement with  $\sigma_s^{(\text{sim})}$ . Then for each cDFT result, we evaluate the bulk pressure in Eq. S48,  $P^{(\text{LHS})}$ , by functional integration together with the pressure correction as presented in the main paper. The right hand side of Eq. S48,  $P^{(\text{RHS})}$ , is evaluated by numerical integration with the equilibrium ionic profiles from cDFT, shown in Fig. S8(c).

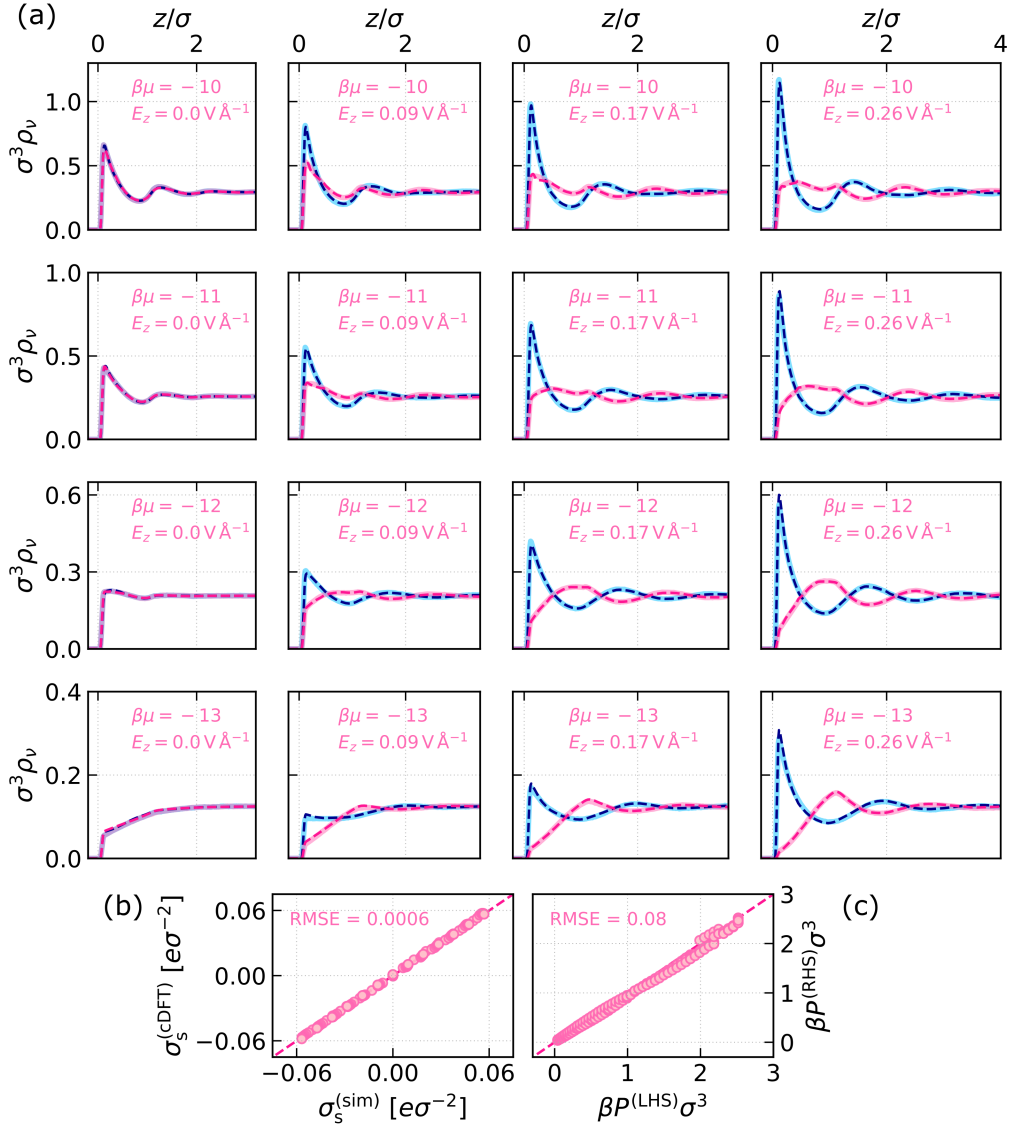


**Figure S8: Electric double layer of the RPM electrolyte in contact with a charged wall.** (a) The equilibrium ion density profiles obtained from finite field simulations (solid lines) and from cDFT (dashed lines). (b) The surface charge densities on the wall obtained from cDFT agree with that from simulation. (c) The cDFT obeys the contact density theorem in Eq. S48, less strictly at high density due to the fixed discretization of the density profiles obtained from cDFT.

## REFERENCES

- <sup>1</sup>A. Z. Panagiotopoulos, "Molecular simulation of phase equilibria: simple, ionic and polymeric fluids," *Fluid Ph. Equilib* **76**, 97–112 (1992).
- <sup>2</sup>A. P. Thompson, H. M. Aktulga, R. Berger, D. S. Bolintineanu, W. M. Brown, P. S. Crozier, P. J. in 't Veld, A. Kohlmeyer, S. G. Moore, T. D. Nguyen, R. Shan, M. J. Stevens, J. Tranchida, C. Trott, and S. J. Plimpton, "LAMMPS - a flexible simulation tool for particle-based materials modeling at the atomic, meso, and continuum scales," *Comput. Phys. Commun* **271**, 108171 (2022).
- <sup>3</sup>S. J. Cox, "Dielectric response with short-ranged electrostatics," *Proc. Natl. Acad. Sci. U.S.A* **117**, 19746–19752 (2020).
- <sup>4</sup>T. Schneider and E. Stoll, "Molecular-dynamics study of a three-dimensional one-component model for distortive phase transitions," *Phys. Rev. B* **17**, 1302–1322 (1978).
- <sup>5</sup>A. Härtel, M. Janssen, S. Samin, and R. v. Roij, "Fundamental measure theory for the electric double layer: implications for blue-energy harvesting and water desalination," *J. Phys. Condens. Matter* **27**, 194129 (2015).

<sup>6</sup>A. Härtel, S. Samin, and R. van Roij, "Dense ionic fluids confined in planar capacitors: in- and out-of-plane structure from classical density functional theory," *J. Phys. Condens. Matter* **28**, 244007 (2016).

<sup>7</sup>J. Jover, A. J. Haslam, A. Galindo, G. Jackson, and E. A. Müller, "Pseudo hard-sphere potential for use in continuous molecular-dynamics simulation of spherical and chain molecules," *J. Chem. Phys* **137**, 144505 (2012).

<sup>8</sup>A. V. Brukhno, J. Grant, T. L. Underwood, K. Stratford, S. C. Parker, J. A. Purton, and N. B. Wilding, "DL\_MONTE: a multipurpose code for Monte Carlo simulation," *Mol. Simul.* **47**, 131–151 (2021).

<sup>9</sup>P. P. Ewald, "Die berechnung optischer und elektrostatischer gitterpotentiale," *Ann. Phys. (Berl.)* **369**, 253–287 (1921).

<sup>10</sup>S. W. de Leeuw, J. W. Perram, E. R. Smith, and J. S. Rowlinson, "Simulation of electrostatic systems in periodic boundary conditions. I. Lattice sums and dielectric constants," *Proc. R. Soc. A* **373**, 27–56 (1997).

<sup>11</sup>R. Hockney and J. Eastwood, *Computer Simulation Using Particles* (Adam-Hilger, 1988).

<sup>12</sup>J. Kolafa and J. W. Perram, "Cutoff errors in the Ewald summation formulae for point charge systems," *Mol. Simul.* **9**, 351–368 (1992).

<sup>13</sup>Q. Yan and J. J. de Pablo, "Hyper-parallel tempering Monte Carlo: Application to the Lennard-Jones fluid and the restricted primitive model," *J. Chem. Phys* **111**, 9509–9516 (1999).

<sup>14</sup>J. K. Johnson, J. A. Zollweg, and K. E. Gubbins, "The Lennard-Jones equation of state revisited," *Mol. Phys.* **78**, 591–618 (1993).

<sup>15</sup>J. M. Rodgers and J. D. Weeks, "Accurate thermodynamics for short-ranged truncations of Coulomb interactions in site-site molecular models," *J. Chem. Phys* **131**, 244108 (2009).

<sup>16</sup>C. Zhang and M. Sprik, "Finite field methods for the supercell modeling of charged insulator/electrolyte interfaces," *Phys. Rev. B* **94**, 245309 (2016).

<sup>17</sup>T. Sayer, C. Zhang, and M. Sprik, "Charge compensation at the interface between the polar NaCl (111) surface and a NaCl aqueous solution," *J. Chem. Phys.* **147** (2017).

<sup>18</sup>T. Sayer, M. Sprik, and C. Zhang, "Finite electric displacement simulations of polar ionic solid-electrolyte interfaces: application to NaCl (111)/aqueous NaCl solution," *J. Chem. Phys.* **150** (2019).

<sup>19</sup>F. Sedlmeier, D. Horinek, and R. R. Netz, "Spatial correlations of density and structural fluctuations in liquid water: A comparative simulation study," *J. Am. Chem. Soc* **133**, 1391–1398 (2011).

<sup>20</sup>R. J. Baxter, "Ornstein–Zernike relation and Percus–Yevick approximation for fluid mixtures," *J. Chem. Phys* **52**, 4559–4562 (2003).

<sup>21</sup>F. Sammüller, S. Hermann, D. de las Heras, and M. Schmidt, "Neural functional theory for inhomogeneous fluids: Fundamentals and applications," *Proc. Natl. Acad. Sci. U.S.A* **120**, e2312484120 (2023).

<sup>22</sup>F. Chollet, *Deep Learning with Python* (Manning Publications, 2017).

<sup>23</sup>J. Dijkman, M. Dijkstra, R. van Roij, M. Welling, J.-W. van de Meent, and B. Ensing, "Learning neural free-energy functionals with pair-correlation matching," (2024), arXiv:2403.15007 [cond-mat.soft].

<sup>24</sup>F. Sammüller and M. Schmidt, "Neural density functionals: Local learning and pair-correlation matching," *Phys. Rev. E* **110**, L032601 (2024).

<sup>25</sup>D. Henderson and L. Blum, "Some exact results and the application of the mean spherical approximation to charged hard spheres near a charged hard wall," *J. Chem. Phys* **69**, 5441–5449 (1978).

<sup>26</sup>D. Henderson, L. Blum, and J. L. Lebowitz, "An exact formula for the contact value of the density profile of a system of charged hard spheres near a charged wall," *J. Electroanal. Chem.* **102**, 315–319 (1979).

<sup>27</sup>P. A. Martin, "Sum rules in charged fluids," *Rev. Mod. Phys.* **60**, 1075–1127 (1988).